Paleoceanography and Paleoclimatology

RESEARCH ARTICLE
10.1029/2020PA003928

Key Points:
- Rapid production of Pb isotope data via laser ablation allows creation of correlated stratigraphic framework for hydrogenetic Fe-Mn crusts
- Pb-Nd data over the last 75 Ma show evolution from restricted basin to open ocean circulation with influence from local continental masses
- Labrador Seawater is present in the east Atlantic basin since 17 Ma and aridification of North Africa can be traced back to 7 Ma

Supporting Information:
- Supporting Information S1

Correspondence to:
P. Josso,
piesso@bgs.ac.uk

Citation:
Josso, P., Horstwood, M. S. A., Millar, I. L., Pashley, V., Lusty, P. A. J., & Murton, B. (2020). Development of a correlated Fe-Mn crust stratigraphy using Pb and Nd isotopes and its application to paleoceanographic reconstruction in the Atlantic. *Paleoceanography and Paleoclimatology*, *35*, e2020PA003928. https://doi.org/10.1029/2020PA003928

Received 16 APR 2020
Accepted 15 SEP 2020
Accepted article online 2 OCT 2020

Development of a Correlated Fe-Mn Crust Stratigraphy Using Pb and Nd Isotopes and Its Application to Paleoceanographic Reconstruction in the Atlantic

P. Josso[1], M. S. A. Horstwood[1], I. L. Millar[1], V. Pashley[1], P. A. J. Lusty[1], and B. Murton[2]

[1]Environmental Science Centre, British Geological Survey, Keyworth, UK, [2]National Oceanography Centre, University of Southampton, Southampton, UK

Abstract Eight ferromanganese crust samples spanning the complete depth range of Tropic Seamount in the northeast Atlantic were analyzed for Pb and Nd isotopes to reconstruct water mass origin and mixing over the last 75 Ma. Pb isotopes were determined by laser ablation multicollector inductively coupled plasma mass spectrometer (LA-MC-ICP-MS), which enables the rapid production of large, high spatial resolution data sets. This makes it possible to precisely correlate stratigraphy between different samples, compare contemporaneous layers, and create a composite record given the abundance of hiatuses in crusts. Pb and Nd isotope data show the influence of various oceanic and continental end-members in the northeast Atlantic Ocean. This reflects its evolution from a restricted, isolated basins in the Late Cretaceous with influxes from the Tethys Ocean, to an increasingly well-mixed, large-scale basin, with a dominant Southern Ocean signature until the Miocene. Less radiogenic Nd isotope signatures suggest Labrador Sea Water influenced the northeast Atlantic basin as early as 17–15 Ma, flowing through a northern route such as the Charlie-Gibbs Fracture Zone. Pb and Nd isotopes highlight the increasing influence of Saharan eolian dust input about 7 Ma, imparting a less radiogenic excursion to the binary mixing between North Atlantic water masses and riverine discharge from West and Central Africa. This highlights the influence of eolian dust input on the open ocean Pb and Nd budget and supports an early stage of North African aridification in the Late Miocene. This signature is overprinted about 3 Ma to the present by a strong North Atlantic Deep Water signature following the onset of Northern Hemisphere glaciation.

1. Introduction

Paleoceanographic reconstructions rely on biological, physical, and geochemical tracers, such as temperature, salinity, and a variety of isotope systems reflecting the effects of geological and climatic phenomena. The radiogenic isotope ratios of Pb and Nd dissolved in seawater, as recorded by authigenic marine precipitates such as ferromanganese (Fe-Mn) encrustations, are a powerful tool for studying water mass mixing and evolution through geological time (Koschinsky & Hein, 2017). Changes in the Pb and Nd radiogenic isotope composition of a water mass can only result from addition from a reservoir with a different isotopic composition as they are unaffected by fractionation induced by biological processes, temperature, and evaporation (Frank, 2002). Accordingly, Pb and Nd isotopes have been frequently used as tracers for studying past water mass mixing and for monitoring continental weathering, because their residence times (50–100 and 600–2000 years, respectively) are shorter than the homogenization time of the ocean (Cochran et al., 1990; Henderson & Maier-Reimer, 2002; Tachikawa, Jeandel, & Roy-Barman, 1999).

This difference in residence time is recognized within the regional Nd isotope signature of water masses that influence different oceanic basins. For example, newly formed North Atlantic Deep Water (NADW) has a signature of −13.5 ε$_{Nd}$ (deviation of the determined $^{143}Nd/^{144}Nd$ ratio from the chondritic uniform reservoir CHUR in parts per 10,000) that originates from the mixing of Labrador Sea Water (LSW: −18 to −14.1 ε$_{Nd}$) with more radiogenic water from the Norwegian-Greenland Sea (NGS: −8 to −11 ε$_{Nd}$) (Figure 1) (Lacan & Jeandel, 2005a; Lambelet et al., 2016; Reynolds et al., 1999). Waters from the Pacific Ocean have a more radiogenic signature (−3 to −5 ε$_{Nd}$), as a result of interaction with younger volcanic

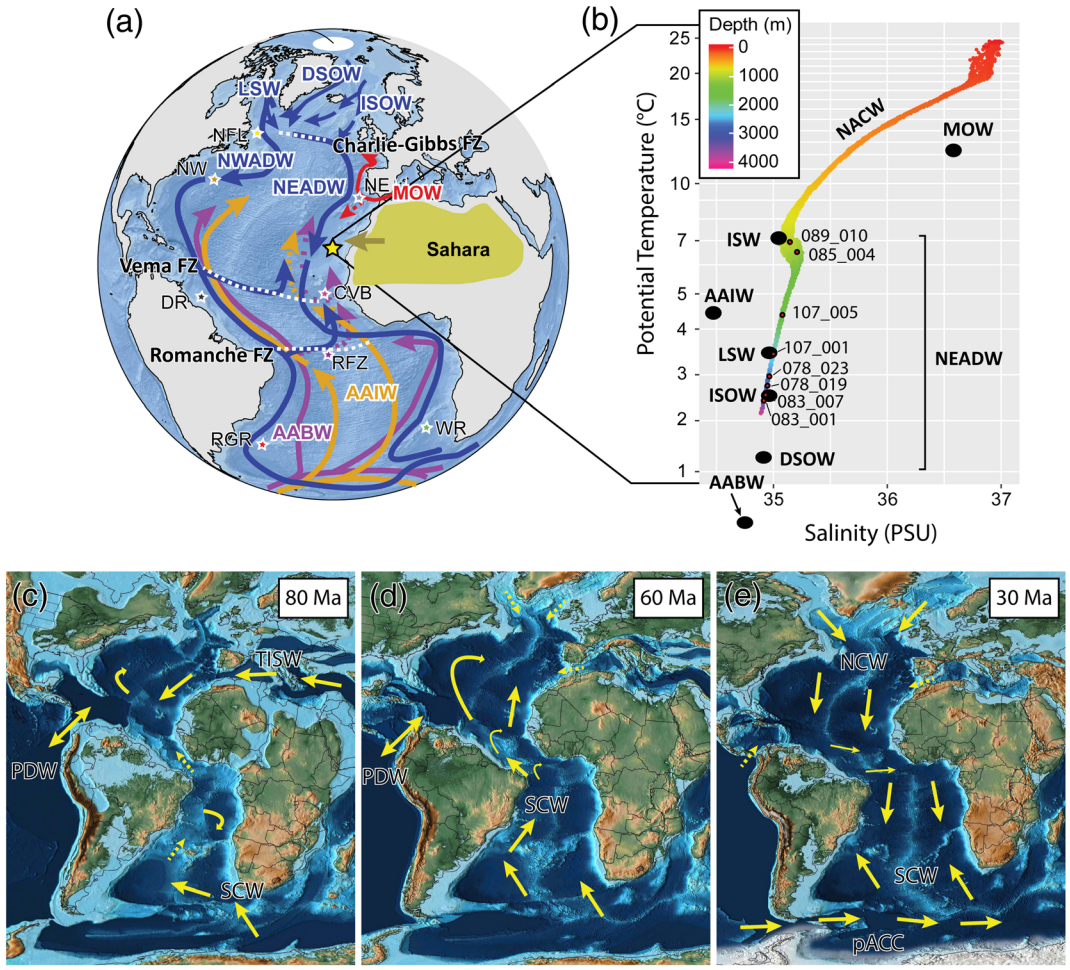

Figure 1. (a) Modern oceanographic circulation in the Atlantic Ocean showing the main intermediate and deep water masses: Labrador Seawater (LSW), Denmark straight overflow water (DSOW), Iceland-Scotland ridge overflow water (ISOW), east and west NADW (ENADW and WNADW, respectively), Antarctic intermediate and bottom water (AAIW and AABW, respectively), and Mediterranean outflow water (MOW). Stars indicate the location of available Nd records used in later figures: NE: northeast Atlantic basin (Muiños et al., 2008); NW: northwest Atlantic basin (Reynolds et al., 1999); RFZ: Romanche Fracture Zone (Frank et al., 2003). Nd data for WR: Walvis Ridge; NFL: Newfoundland; RGR: Rio Grande Rise; DR: Demerara Rise; and CVB: Cape Verde Basin are from a compilation by Thomas and Via (2006) and Batenburg et al. (2018). (b) Temperature versus salinity (practical salinity unit) data from CTD deployments during the JC142 MarineE-Tech mission in 2016. Water mass end-members from Jenkins et al. (2015). (c–e) The paleoceanographic reconstruction (modified from Scotese, 2016) of the Atlantic basin at 80, 60, and 30 Ma, respectively. These depict the major tectonic evolution of the basin and dominant water masses of these periods (TISW: Tethyan Indian Saline Water; SCW: Southern Component Water; PDW: Pacific Deep Water; pACC: proto-Antarctic Circumpolar Current).

rocks (Scher & Martin, 2008). Mixing of NADW with Pacific water, with a further contribution from highly diverse Antarctic terranes, leads to Antarctic bottom and intermediate waters (AABW and AAIW, respectively) having intermediate ƐNd values (−7 to −9) (Flierdt et al., 2016; Reynolds et al., 1999; Scher et al., 2015). This progressive mixing supports the quasi-conservative behavior of Nd in the ocean (Flierdt et al., 2016). Therefore, temporal variations in Nd isotopic composition at a given location result from changes in the contribution of deep waters from a particular source region (water mass mixing), or changes in the composition of Nd drained from the deep water source region (weathering) (Thomas & Via, 2006). In such context, less radiogenic Nd signatures tend to designate old continental rocks, while young mantle rocks, such as newly formed basaltic crust, have radiogenic Nd signatures due to higher Sm/Nd ratio in depleted mantle rocks (Frank, 2002). While the general relationship between continental

lithologies and regional seawater signature is now clear, other processes emerge as important local parameters effecting the Nd budget and signature of seawater along continental margins. This is notably the case of seawater interaction with sediments where sorption-desorption processes balance the isotopic signature of seawater through dissolution and precipitation of particles (Flierdt et al., 2016; Jeandel et al., 2007). The discharge of submarine groundwater and benthic fluxes from pore waters are also recognized as additional sources of Nd in the ocean (Abbott et al., 2016; Johannesson & Burdige, 2007).

In contrast, Pb isotope signatures are more spatially diverse, as a consequence of Pb shorter residence time in the ocean. Therefore, it reflects the influence of local inputs, such as the intensity and type of weathering taking place (e.g., mechanical or chemical), because of the incongruent release of Pb during chemical weathering of continental rocks (Blanckenburg & Nägler, 2001) as a result of the preferential dissolution of U-containing accessory minerals (Harlavan & Erel, 2002). Such processes result in enhanced radiogenic signatures of the weathered product. Contrary to the Nd system, old cratonic terranes usually have more radiogenic signatures compared to younger volcanic or sedimentary rocks (Harlavan & Erel, 2002). Consequently, the secular variation in Pb isotopes can reflect changes in the weathering style of a given source, such as glacial–interglacial cycles (Foster & Vance, 2006), changes in the provenance of weathering products (mixing), or a combination of both.

Over the last few decades, deep-sea Fe-Mn crusts have been extensively studied to retrace historical water conditions in all the planet's oceans (Frank, 2002; Godfrey, 2002; Goto et al., 2017; Josso et al., 2020; Konstantinova et al., 2017; Mizell, Hein, Lam, et al., 2020; Muiños et al., 2008; Nishi et al., 2017; Rehkämper et al., 2004). Due to their extremely slow accumulation rate (a few mm/Ma), these marine precipitates provide a low-resolution, but long-term, archive of seawater chemistry (Koschinsky & Hein, 2017).

This study uses a suite of hydrogenetic Fe-Mn crusts spanning the entire depth range (1,000–3,800 m below sea level) of Tropic Seamount in the northeast Atlantic (Figure 2), to study water mass distribution and mixing using Pb and Nd isotopes. A detailed age model for one of the samples has recently been produced, using Bayesian statistical modeling of Markov Chain Monte Carlo simulations, combining Os isotope data, U-Pb dating and Co-chronometry (Josso et al., 2019). This age model shows that Core 085_004 preserves Fe-Mn crust deposition spanning the last 75 $\pm$ 2 Ma and, therefore, offers an opportunity to study the evolution of the circulation and weathering inputs to the northeast Tropical Atlantic over most of the Cenozoic and Late Cretaceous (Figure 1).

Throughout its tectonic evolution, major closing and opening of oceanic gateways as well as opening of new minor basins changed the origin and hydrographic regime of the Atlantic Ocean (Figure 1). In the Late Cretaceous, the circulation in the North Atlantic was dominated by influx from the Pacific and Tethyan seaway with minor contributions of Southern Component Water (SCW) through the equatorial Gateway (Mourlot et al., 2018). The less vigorous influx of deep water and more sluggish circulation conditions of the Late Cretaceous suggest the potentially stronger influence of local nearshore processes on water masses isotopic signatures (Pérez-Díaz & Eagles, 2017). Around the Cretaceous-Paleocene boundary, limited deep water formation initiated in the high latitudes of the North Atlantic and Pacific Ocean (Pérez-Díaz & Eagles, 2017). The Paleocene marks a major period of widening and deepening of the equatorial gateway, of other oceanic basins of the Atlantic Ocean, and the onset of near modern thermohaline circulation patterns with major latitudinal water mass movements dominated by meridional sources (Figure 1) (Batenburg et al., 2018). In the Oligocene, the opening of the Drake Passage and deepening of the Tasman Strait about 33–29 Ma triggered a reorganization of the currents in the southern hemisphere establishing the Antarctic Circumpolar Current (ACC) (Katz et al., 2011; Scher & Martin, 2008). The transition to a bipolar mode of deep-ocean current formation occurred around a similar period to the onset of the ACC, although estimates vary from Ealry Oligocene to Middle Miocene (Scher & Martin, 2008; Thomas & Via, 2006; Wright et al., 1992; Wright & Miller, 1996; Zachos et al., 2001). Earliest production of deep water in the North Atlantic, Northern Component Water (NCW), initiated in the Early Oligocene with the deepening of sills previously isolating the Arctic, Greenland, and Norwegian basins from the North Atlantic (Batenburg et al., 2018). The NCW evolved progressively to its current NADW signature (salinity, temperature, and isotopic composition) over the last 3–4 Ma with the increased deep water generation in the Labrador Sea, with unique isotopic features derived from the weathering of Archean shield units by Northern Hemisphere Glaciation episodes (Thomas & Via, 2007).

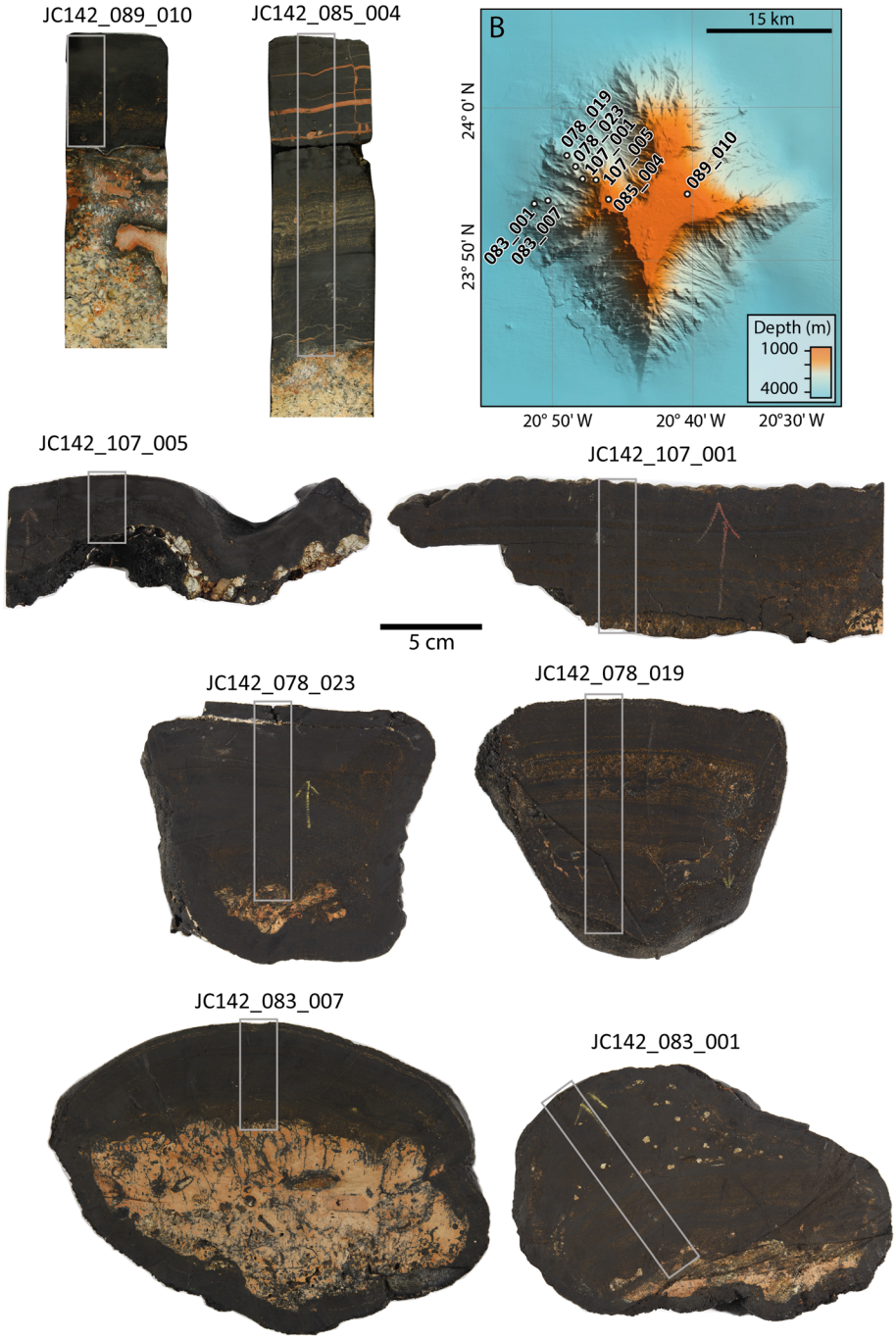

Figure 2. Cut Fe-Mn crust samples used in this study and their location on Tropic Seamount (Table 1). Bathymetric map of Tropic Seamount obtained from the ship-based EM120 during JC142, gridded at 50 m and showing the location of Fe-Mn crust samples (modified from Yeo et al., 2018). The gray rectangles represent the stratigraphic portions used to create thin sections for SEM observations and LA-MC-ICP-MS analysis. All samples are presented at the same scale.

Most oceanographic studies of the Atlantic have focused on the north and northwest basin given the predominance of deep water formation in these regions and global circulation pattern. Therefore, the research presented herein offers a complementary view from the less documented northeast Atlantic basin, yielding Pb and Nd isotope data for the last 75 Ma. This record is essential to reconstruct water mass circulation in this region in conjunction to the major climate transition of the Cenozoic from hot to ice house.

Table 1
Location, Depth, and Thickness of the Eight Fe-Mn Crust Samples From Tropic Seamount Used in This Study

Sample #	Latitude		Longitude		Depth (mbsl)	ROV tool	Fe-Mn thickness (mm)
	Deg	Dec. min.	Deg	Dec. min			
JC142_078_019	23	56.561	−20	48.723	3,101	Manipulator arm	105
JC142_078_023	23	55.978	−20	48.394	2,822	Manipulator arm	95
JC142_083_001	23	53.343	−20	51.390	3,777	Manipulator arm	130
JC142_083_007	23	53.348	−20	50.888	3,512	Manipulator arm	54
JC142_085_004	23	53.768	−20	46.056	1,130	Rock drill	145
JC142_089_010	23	54.288	−20	40.552	1,028	Rock drill	55
JC142_107_001	23	55.254	−20	47.817	2,330	Manipulator arm	85
JC142_107_005	23	55.221	−20	47.265	1,803	Manipulator arm	30

2. Material and Methods

2.1. Geological Context

Tropic Seamount is part of the Saharan Seamount Province (SSP), located 450 km from the passive continental margin of West Africa, halfway between the Canary and Cape Verde islands (Josso et al., 2019). Tropic Seamount is emplaced over 155 Ma oceanic crust and formed principally during the late Aptian (119–114 Ma), with minor volcanic activity occurring until the Middle Paleocene (van den Bogaard, 2013).

Tracing the subsidence of Tropic Seamount since its formation (119–114 Ma) on the 155 Ma oceanic crust using the thermal subsidence model defined by Crosby and Mckenzie (2009) for Atlantic oceanic crust and combined with eustatic variations (Haq, 2014; Haq et al., 1987), indicates the major part of Tropic Seamount subsidence occurred over its first 40 Ma of existence (120–80 Ma) (supporting information Figure S1). Indeed, most of the oceanic crust subsided from 155 to 80 Ma to then stabilize and partially rebound (Crosby & Mckenzie, 2009). Thereafter, most changes in depth of the Fe-Mn crust samples are driven by short-term eustatic variations (Haq, 2014, Haq et al., 1987) overprinting a long-term rebound of the oceanic crust (supporting information Figure S1). A maximum amplitude of variation of 260 m, ranging from 900–1,160 mbsl for the summit Sample 085_004 (75–0 Ma; Figure 2), can be deduced tracing the paleodepth of the sample through time. Thus, we do not consider subsidence the primary driver of isotopic variations in our samples.

2.2. Fe-Mn Crust Samples

The samples for this study were recovered during the JC142 expedition of the NERC-funded "MarineE-Tech" project to Tropic Seamount in 2016, by the remotely operated vehicle (ROV) Isis (Figure 2). Samples from the western flanks of Tropic Seamount were recovered using the ROV manipulator arms, while Fe-Mn crust pavement samples from the summit were obtained in situ using a ROV-mounted drill. The samples have thicknesses ranging from 30 to 145 mm (Table 1 and Figure 2). Previous geochemical analysis indicate that shallow samples, older than 38 Ma are phosphatised (Josso et al., 2019, 2020), a feature not present in deeper samples. This particularity offers the possibility to evaluate the influence of secondary diagenetic phosphatization on the integrity of isotopic records in contemporaneous layers of Fe-Mn crusts.

2.3. SEM Imaging

All measurements were carried out on a 100 μm carbon-coated (25 nm thick) polished thin sections following the stratigraphic sections highlighted in Figure 2. Backscatter electron (BSE) imaging was performed on an FEI Quanta 600 scanning electron microscope (SEM) fitted with an Oxford Instruments INCA Energy 450 X-ray microanalysis system. All BSE images reflect the original stratigraphic orientation of the sample.

2.4. Pb and Nd Isotope Solution Measurements

Thirty-eight microdrilled subsamples were recovered from Sample 085_004 and analyzed for Pb and Nd isotopes. An additional 40 microdrilled subsamples were recovered from Samples 078_019 and 107_001 for Nd

isotope analysis. All powdered subsamples were leached in closed vessels using 2.5 M HCl on a hot plate for 8 hr to target the Fe-Mn oxides (+ carbonates and easily leachable adsorbed species) and leaves the residual silicates intact. The liquid phase was extracted following centrifugation and the solute separated into two aliquots for Nd and Pb column chemistry at the BGS Geochronology & Tracers Facility (GTF). Pb was separated using standard anion exchange chemistry using Eichrom AG1x8 resin. Rare earth elements were concentrated using columns packed with Eichrom AG50x8 cation exchange resin, and Nd was then separated using Eichrom LN-SPEC resin.

Pb and Nd solution isotope measurements were performed using a ThermoScientific Neptune Plus multicollector inductively coupled plasma mass spectrometer (MC-ICP-MS) coupled to a Teledyne-Cetac Technologies Aridus II desolvating nebulizer and an ESI SC-microautosampler with PFA-50 nebulizer tip. Each acquisition consisted of 75 ratio measurements, collected at 4 s integrations, following a 60 s electronic baseline. Repeatability and bias of the measurements were assessed through regular analysis of JNdi and NBS 981 Nd and Pb reference solutions. Prior to Pb isotope analysis, each sample was spiked with a thallium solution, which allowed for the correction of instrument-induced mass bias. Nd was corrected for mass fractionation using $^{146}Nd/^{144}Nd = 0.7219$. The data are normalized to the values of Tanaka et al. (2000) and Baker et al. (2004) for Nd and Pb, respectively. For Nd, analysis of additional secondary reference materials Nod-A-1, Nod-P-1, JMn-1, and a homemade reference material (HRM) over four analytical sessions yielded the following results (weighted average ±95% conf): −9.68 ± 0.19 ƐNd for Nod-A-1 ($n = 5$), −3.93 ± 0.20 ƐNd for Nod-P-1 ($n = 5$), −5.80 ± 0.15 ƐNd for JMn-1 ($n = 3$), and −11.63 ± 0.33 ƐNd for our HRM ($n = 3$) (supporting information Table S1, https://doi.org/10.5285/ce4cd06e-ada2-4c2b-89cf-2f0f81884396). These results are within uncertainty of the range of reported values for Nod-A-1 (−9.55 to −9.91 ƐNd [$n = 3$]), and Nod-P-1 (−4.02 to −4.25 ƐNd, $n = 4$) (Jochum et al., 2005). To our knowledge these are the first reported ƐNd values for JMn-1.

After normalization and uncertainty propagation to NBS981, solution Pb isotope validation data for Nod-A-1, Nod-P-1, JMn-1 and HRM, are within uncertainty of reference values (Table 2).

2.5. LA-MC-ICP-MS Measurements

To maintain consistent analytical conditions between reference materials and sample thin sections, the powdered reference materials were mixed with resin, mounted on a glass-slide and then polished to produce flat surface for laser ablation (LA). Wax-bound pressed pellets were found to have an erratic ablation behavior during ablation tests.

LA work was performed using an Elemental Scientific Lasers NWR193UC LA system with TV2 two-volume ablation cell, coupled to a ThermoScientific Neptune Plus MC-ICP-MS. Data were collected on a continuous time-resolved basis, with data integrated every 0.262 s. Data were processed manually to correct for the differential tau response of the Faradays, which impacted the data due to the large signal variations experienced from integration to integration, before further processing and normalization using the Iolite (v.3.65) data reduction software (Paton et al., 2011). Fe-Mn crust samples were analyzed using a letter box format ablation pattern of 15 * 150 μm continuously rastering at 10 μm/s perpendicular to the sample's stratigraphy. LA Pb isotope ratios were normalized through standard bracketing using the Baker et al. (2004) values for Nod-A-1 as the primary reference material and also propagated for any overdispersion in the Nod-A-1 data for each analytical session. Validation data are presented in Table 2. Nod-A-1 measurements ($n = 162$) were performed during nine sessions spread over 8 months. After normalization and propagation, the validation materials Nod-P-1, JMn-1, and HRM show no scatter within or between analytical sessions, demonstrating appropriate uncertainty propagation relative to the overdispersion of Nod-A-1. LA Pb isotope data for Nod-P-1, JMn-1, and HRM deviate from solution results by 0.0019–0.0442%, 0.0150–0.0712%, and 0.0048–0.0212%, respectively (see Table 2). It is noticeable that HRM exhibits better agreement than Nod-P-1 and JMn-1. The HRM was ground to a finer-grain size (95% < 32 μm and >99% < 53 μm) during preparation at the BGS laboratories and is therefore likely more homogeneous than Nod-P-1 and JMn-1. The sample LA data presented here is averaged every 20 integrations and consequently, each data point represents the Pb isotopic composition measured over 50 μm. A comparison of the laser and solution Pb isotope data is provided in supporting information Figure S2.

Table 2
Pb Isotope Solution and Laser Ablation Validation Data for Fe-Mn Crust Reference Materials and a Homemade Reference Material Developed During This Study

		$^{206}Pb/^{204}Pb$	2 s%	$^{207}Pb/^{204}Pb$	2 s%	$^{208}Pb/^{204}Pb$	2 s%	$^{208}Pb/^{206}Pb$	2 s%	$^{207}Pb/^{206}Pb$	2 s%
Nod-A-1	solution	18.9639	0.0064	15.6857	0.0071	38.9568	0.0085	2.05428	0.0041	0.827135	0.0021
	Baker et al. (2004)	18.9640	0.0034	15.6850	0.0064	38.9560	0.0075	2.05430	0.0082	0.827090	0.0072
	GeoREM	18.957–18.964		15.675–15.685		38.929–38.952		2.0542–2.0543		0.82705–0.82709	
Nod-P-1	solution	18.7068	0.0061	15.6405	0.0068	38.6941	0.0081	2.06847	0.0041	0.836089	0.0020
	Baker et al. (2004)	18.7000	0.0323	15.6380	0.0170	38.6970	0.0216	2.06936	0.0389	0.836257	0.0365
	GeoREM	18.697–18.7081		15.629–15.638		38.669–38.699		2.06850		0.835800	
	laser ablation (n = 44)	18.7029	0.0150	15.6336	0.0115	38.6895	0.0132	2.06854	0.0073	0.835821	0.0095
	LA/Baker et al. (2004)	*1.000155*		0.999718		0.999806		0.999605		0.999479	
	LA/soln	*0.999791*		0.999555		0.999881		1.000036		0.999680	
JMn-1	solution	18.7677	0.0063	15.6440	0.0071	38.7518	0.0085	2.06483	0.0042	0.833562	0.0020
	laser ablation (n = 44)	18.7579	0.0112	15.6343	0.0109	38.7244	0.0147	2.06449	0.0063	0.833423	0.0048
	LA/soln	0.999480		0.999378		0.999293		0.999834		0.999833	
HRM	solution	18.8836	0.0063	15.7052	0.0071	39.0231	0.0085	2.06653	0.0041	0.831684	0.0019
	laser ablation (n = 69)	18.8819	0.0085	15.7019	0.0083	39.0147	0.0121	2.06640	0.0048	0.831569	0.0037
	LA/soln	0.999914		0.999793		0.999784		0.999938		0.999862	

Note. Data from Baker et al. (2004) and the GEOREM database (Jochum et al., 2005) are provided for comparison.

3. Results

3.1. Pb Isotope Correlated Stratigraphy

The continuous Pb isotope LA profiles from crust samples spanning a depth range of 1,028–3,777 mbsl are shown on a schematic west-east topographic section of Tropic Seamount (Figure 3). The age model developed for Core 085_004 (Josso et al., 2019) is used in conjunction with prominent isotopic excursions in the Pb isotope record to transpose the age model and temporally correlate samples from the summit to the abyssal plain. The $^{207}Pb/^{206}Pb$ ratio is primarily used for this correlation due to its high precision and large variation in amplitude (Figure 3 and supporting information Figures S3–S6). A similar correlation with detailed images of textures is provided in supporting information Figure S7. Following the correlation presented in Figure 3, the isotopic trends are plotted against time in Figure 4, therefore deleting the distorting effect of varying growth rates between samples.

Figure 4 makes it possible to compare temporally matching portions of the record from different depths and establish a composite Pb isotope record for Tropic Seamount. Portions showing the best record continuity, over the longest periods of time, and with the least mineral texture disruptions or disturbance by detrital material were selected for the composite record (highlighted in red in Figures 3 and 4). Although Sample 085_004 shows the most complete isotopic record overall, the low abundance of Fe-Mn oxides in the Oligocene and Late Miocene (Figures 3 and 4 and supporting information Figure S7; Josso et al., 2020) as well as the numerous minor erosive surfaces in the Pliocene (5.3 ± 1.7–2.5 ± 1.9 and 1.2 ± 0.3–0 Ma; Josso et al., 2019) leads to the consideration of isotopic records from other samples for these periods.

The samples from deeper water depths show no sign of phosphatization and contain a greater abundance of Fe-Mn oxides and less carbonates, as evidenced by the mosaicked SEM profiles (Figure 3 and supporting information Figure S7). Accordingly, the section from 078_023 is used to construct the composite record of the Eocene and Oligocene, while 107_001 is used for the most recent record showing no hiatuses and well-developed stratigraphy. The resulting composite Pb record for Tropic Seamount (supporting information Table S2; https://doi.org/10.5285/ce4cd06e-ada2-4c2b-89cf-2f0f81884396) is plotted against time together with other records from the Atlantic Ocean for comparison (Figure 5) and used for further discussion.

3.2. Composite Pb Isotopes Time Series

In general, the $^{206,\ 207,\ 208}Pb/^{204}Pb$ ratios have similar trends, mirrored by variations in the $^{208,\ 207}Pb/^{206}Pb$ ratios (Figure 5). The Late Cretaceous is characterized by the peak radiogenic values observed at Tropic Seamount ($^{206,\ 207,\ 208}Pb/^{204}Pb$ = ~19.18, ~39.25, ~15.79, and $^{208,\ 207}Pb/^{206}Pb$ = ~2.043, ~0.822, respectively). The Pb isotope data then decline to less radiogenic values in a stepwise pattern, coincidental with the Cretaceous-Paleogene and Paleocene-Eocene boundaries ($^{206,\ 207,\ 208}Pb/^{204}Pb$ = ~18.75, ~38.75, ~15.63, and $^{208,\ 207}Pb/^{206}Pb$ = ~2.043, ~0.822, respectively). The general trend of the Pb isotope data then returns to more radiogenic values across the Oligocene and Miocene up to ~10 Ma. Over the last 10 Ma, Pb isotopes present a saw tooth pattern, with less radiogenic excursions at 5 and 3 Ma, which are most evident in Samples 089_010, 107_005, and 107_001 (Figures 3–5). The 0–3 Ma period shows a rapid excursion to more radiogenic values in the $^{206,\ 208}Pb/^{204}Pb$ ratios, while the $^{207}Pb/^{204}Pb$ remains constant over this period, in good agreement with triple-spiked Pb data from Abouchami et al. (1999).

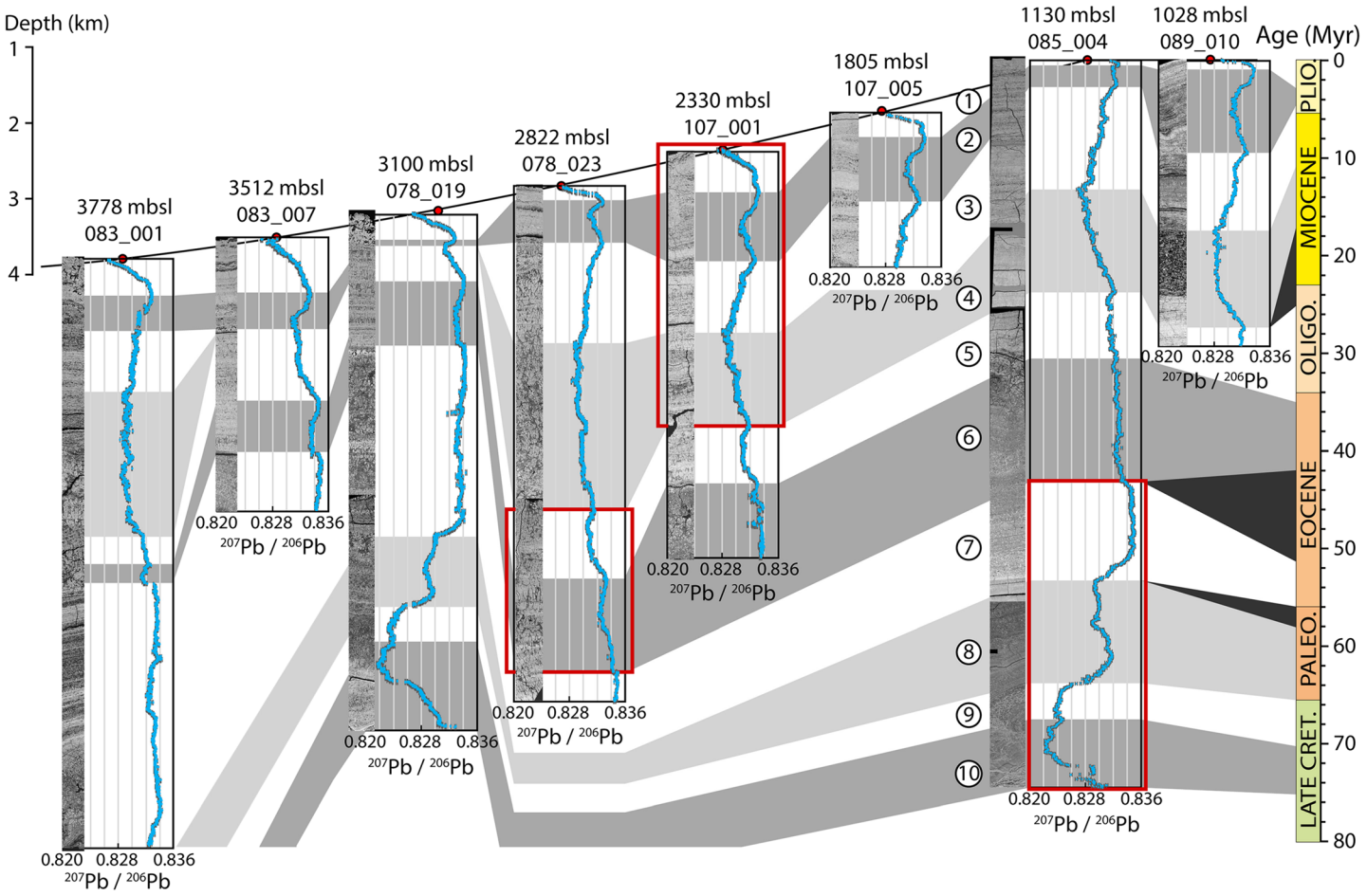

Figure 3. Correlation of the stratigraphy of Fe-Mn crusts samples from Tropic Seamount using LA-MC-ICP-MS Pb isotope data and the age model developed for Core 085_004 (Josso et al., 2019). Circled numbers (1–10) represent the various layers identified visually for their unique Pb isotope trends and highlighting the stratigraphy. The black areas represent hiatuses in the age model for Core 085_004 for which no complementary record was identified in adjacent samples. Electron backscatter images, acquired with an FEI Quanta 600 SEM with a 20% surface overlap, were mosaicked to produce a continuous stratigraphic transect of each thin section, using Image Composite Editor©. Similar correlated stratigraphy for other Pb isotope ratios and textures are presented in supporting information Figures S3–S6, while Figure S6 presents a detailed view of the textures.

Pb isotope signatures of the surface of the eight Fe-Mn crust samples vary from 18.9–19.0, 15.67–15.71, 39.05–39.1, 0.826–0.831, and 2.056–2.068 for $^{206,\ 207,\ 208}Pb/^{204}Pb$ and $^{207,\ 208}Pb/^{206}Pb$, respectively. This is consistent with reported values for Fe-Mn crusts surface scrapes from the Atlantic (Abouchami et al., 1999; Frank et al., 2002, 2003; Muiños et al., 2008). There is a systematic trend toward less radiogenic values with increasing water depth of the samples (Figure 4), which relates to erosive conditions on the summit of Tropic Seamount (Yeo et al., 2019) and loss of the most recent, more radiogenic part of the record in some samples.

In Pb-Pb space (Figure 6), the composite Pb record does not plot as a straight line but rather defines five to six distinct trends corresponding to the period 75–58, 56–25, 17–7, 7–3, and 3–0 Ma. Each trend can be interpreted as approximate binary mixing between two end-member sources. Plotting the complete Pb data set, trends, and signature of end-members relevant to the study area (Figures 6g and 6h) highlights that a mixture of the cratonic terranes of South America (Amazon and Orinoco sediments) and West Africa (Congo River fan sediment) dominate the radiogenic end-member of the record. The less radiogenic end of our data plots in an intermediate position between the signature of the Tethys and that of SCW. Divergences between trends remain minimal over the period 75–7 Ma and highlight a remarkably stable Pb isotope mixing trend from the Late Cretaceous to the Messinian, which demonstrate the strong local continental source of Pb to Tropic Seamount throughout most of the Cenozoic.

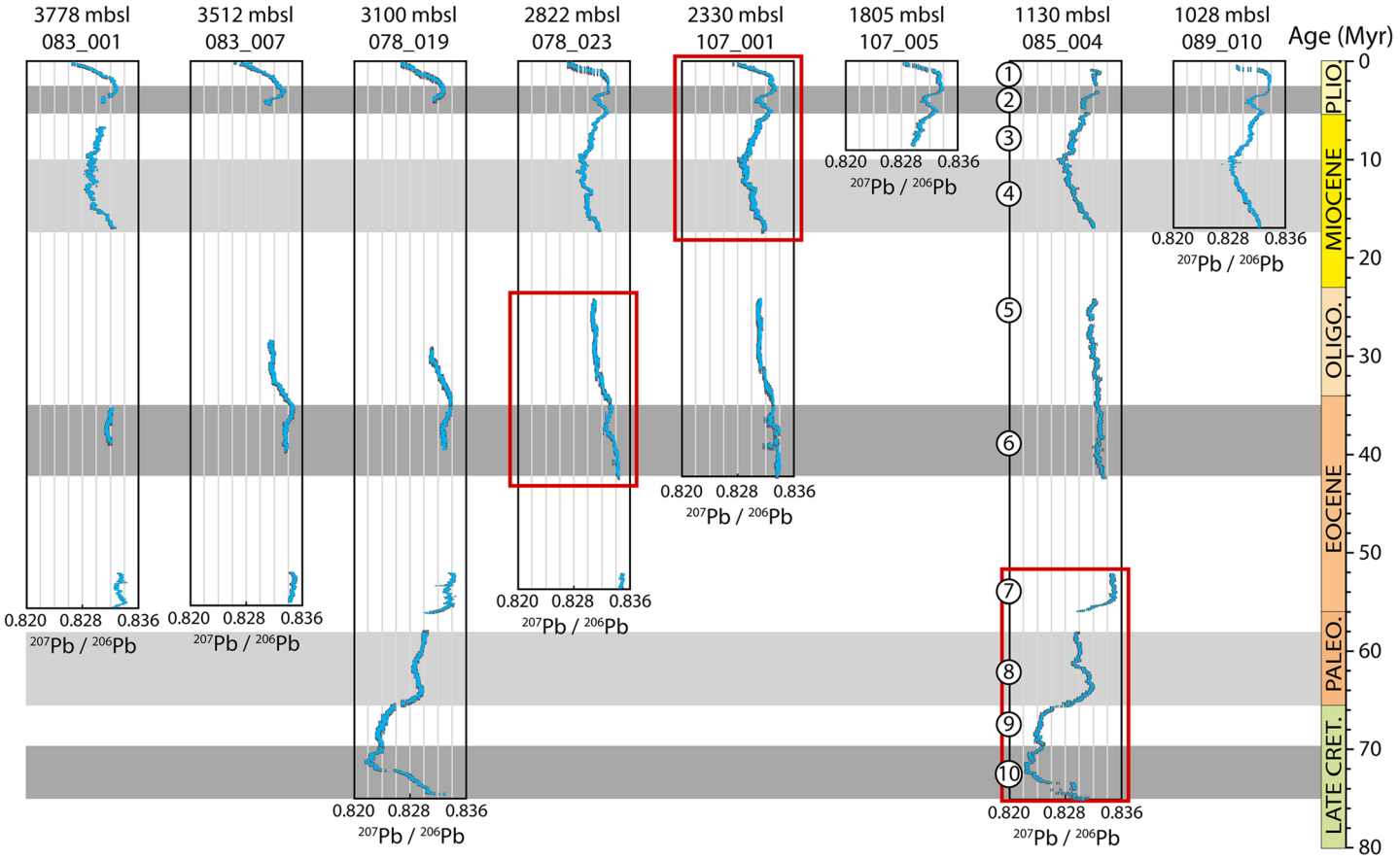

Figure 4. LA-MC-ICP-MS Pb isotope data plotted against a linear timescale.

3.3. Nd Isotope Time Series

The Nd isotope data obtained from the Fe-Mn crust samples are available in the supporting information (Table S3; https://doi.org/10.5285/ce4cd06e-ada2-4c2b-89cf-2f0f81884396). The Nd data for Samples 085_004 and 078_019 are distinctive in the Late Cretaceous (Figure 78). Both initiate at −11 ƐNd, but the deeper water sample increases to more radiogenic values (−10.3 ƐNd), which remain constant until the end of the Paleocene. This trend is similar to that of the Tethys, albeit it 1.5 ƐNd unit less radiogenic than Tethys values (Pucéat et al., 2005; Figure 7). In contrast, the shallower water sample presents a major radiogenic excursion, reaching up to −9.3 ƐNd at about 61 Ma. This excursion corresponds to an average increase of 0.3 ƐNd per Ma between 67 and 61 Ma and indicates a vertically stratified water column, separating intermediate and surface water from a deeper Tethys-influenced water mass. Both samples have similar values for the Early Eocene, decreasing to a minima of −10.5 to −10 ƐNd at 54 Ma. In the late Eocene and Oligocene the data from all three water depths converge toward less radiogenic values. This trend begins about 36 Ma for the deeper sample, while it initiates 32 Ma ago in the other two. Given the absence of depth change in relation to subsidence and eustatic variations over this period (supporting information Figure S1), this indicates it took 3–4 Ma for the upper limit of the deeper water mass to shoal and effect the isotopic signature of the intermediate and shallow sample. Over the last 17 Ma, the ƐNd time series evolved from −10.2 to −11.9 ƐNd, although diachronous between the intermediate and shallow water sample from about 7–8 Ma ago. The Nd isotope signatures obtained from the surface of Samples 107_001 (−11.35 ± 0.26 ƐNd) and 078_019 (−11.9 ± 0.3 ƐNd) are consistent with current seawater values reported for this region (Jenkins et al., 2015; Rickli et al., 2009; Schlitzer et al., 2018).

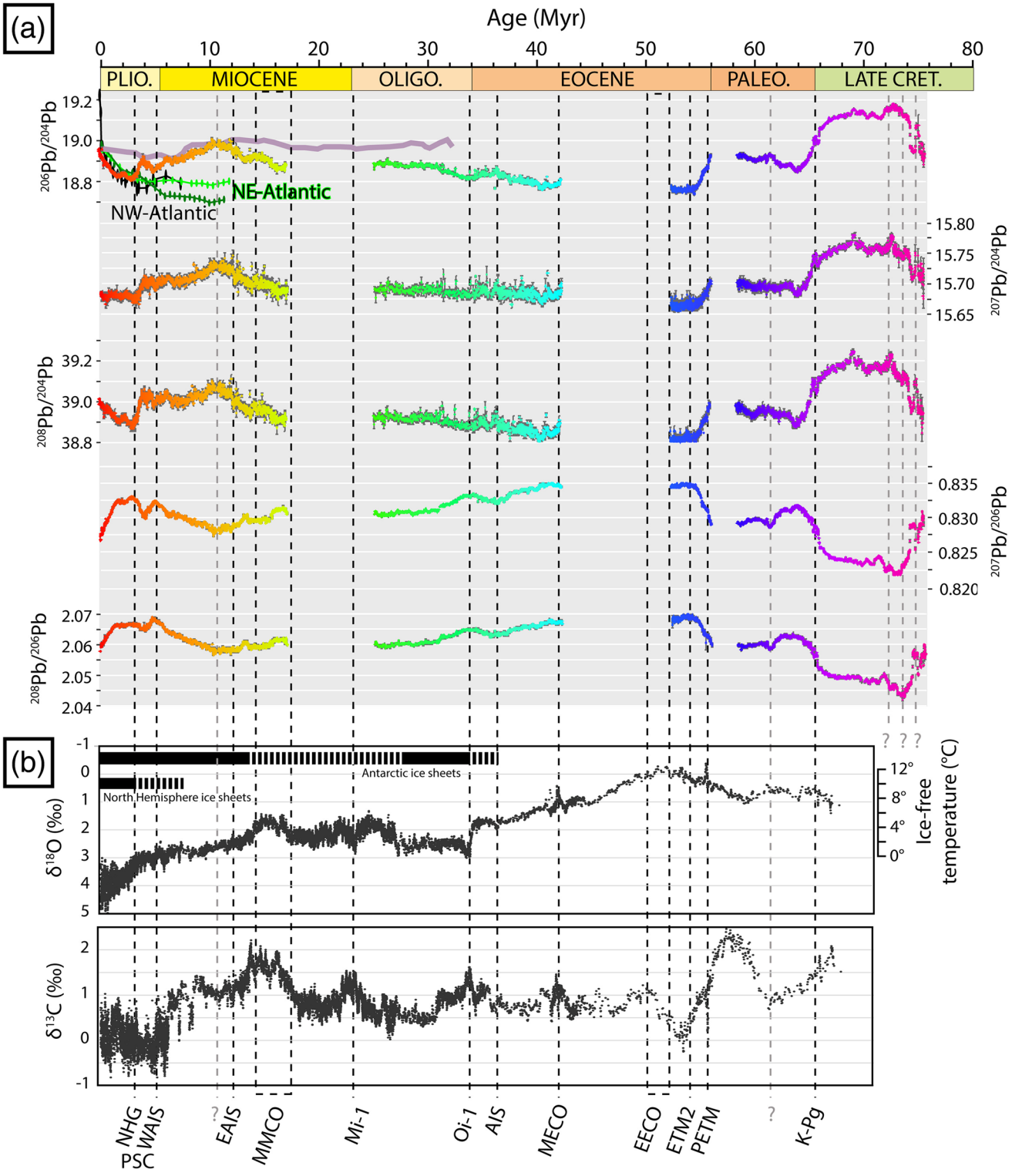

Figure 5. (a) Time series of the composite Pb isotope record from Tropic Seamount, color coded linearly for age to aid representation in Figure 6. (b) Global deep-sea oxygen and carbon isotope records based on data from Zachos et al. (2008). Major events of the Cenozoic (Zachos et al., 2001) are highlighted: K-Pg: Cretaceous-Paleogene meteor Impact and Deccan Trap Volcanism; PETM: Paleocene-Eocene Thermal Maximum; ETM2: Eocene Thermal Maximum 2; EECO and MECO: Early and Mid-Eocene Climatic Optimum; AIS: Antarctic Ice Sheets; Oi-1: Oligocene glaciation; Mi-1: Miocene glaciation; MMCO: Mid-Miocene Climatic Optimum; E-WAIS: East and West Antarctic Ice Sheets development; PSC: Panama Seaway Closure; NHG: Northern Hemisphere Glaciation. Data from the NE Atlantic basin from Muiños et al. (2008), NW Atlantic data on sample BM1969.05 from Reynolds et al. (1999), RFZ: Romanche Fracture Zone from Frank et al. (2003), and previously published data on sample 121DK from Tropic Seamount from Abouchami et al. (1999).

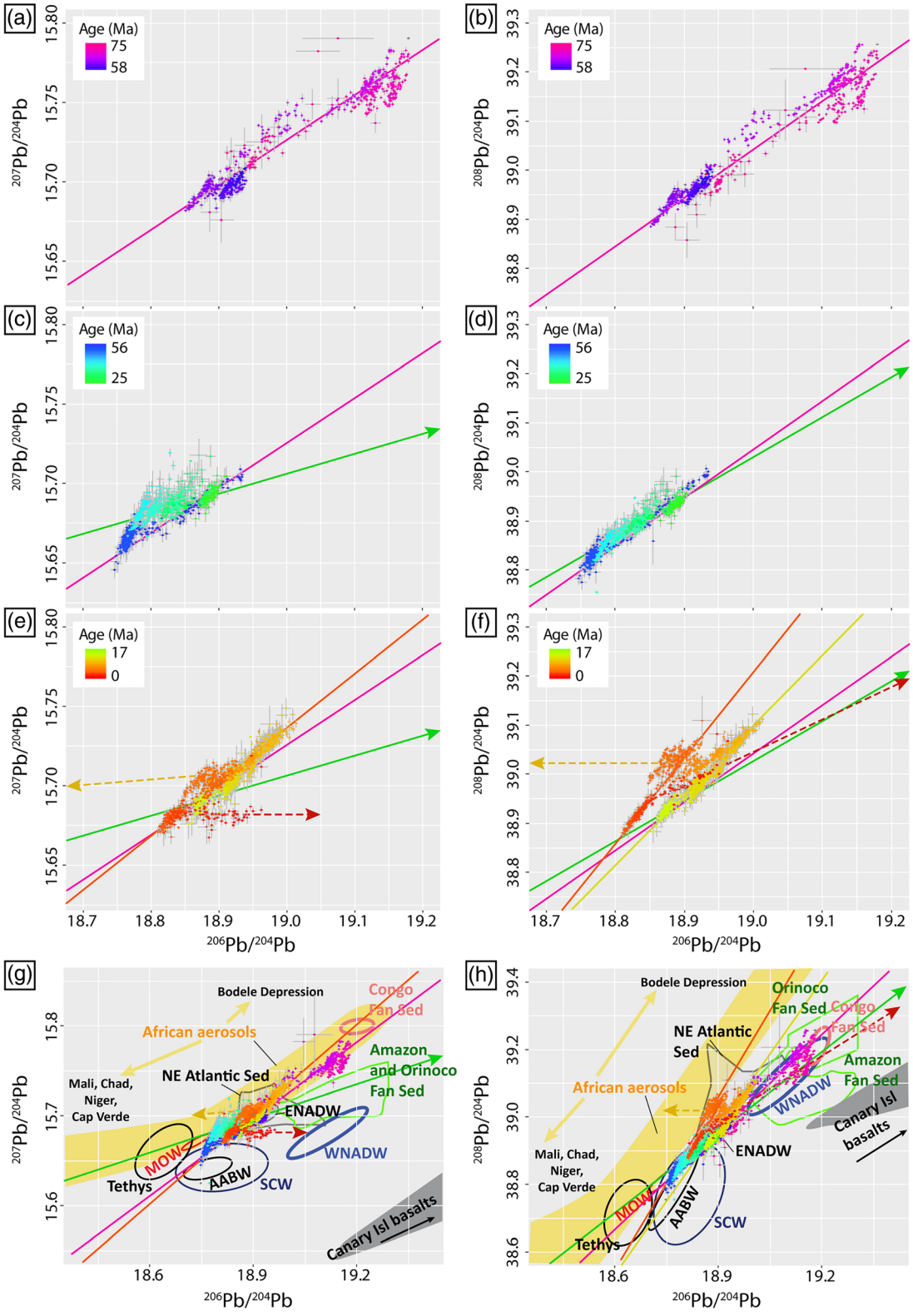

Figure 6. $^{207}Pb/^{204}Pb$ versus $^{206}Pb/^{204}Pb$ and $^{208}Pb/^{204}Pb$ versus $^{206}Pb/^{204}Pb$ diagram of laser ablation data for the composite record for the 75–58 Ma (a and b), 56–25 Ma (c and d), and 17–0 Ma (e and f) periods using similar color coding to Figure 5. In each panel, the major trends form by the data are highlighted with a colored line representative of the period. Panels (g) and (h) present the complete composite records and trends with potential source end-member signatures from Sun et al. (1980), Christensen et al. (1997), Abouchami et al. (1999), Frank et al. (2003), Millot et al. (2004), Muiños et al. (2008), Abouchami et al. (2013), Kumar et al. (2014), and Kumar et al. (2018).

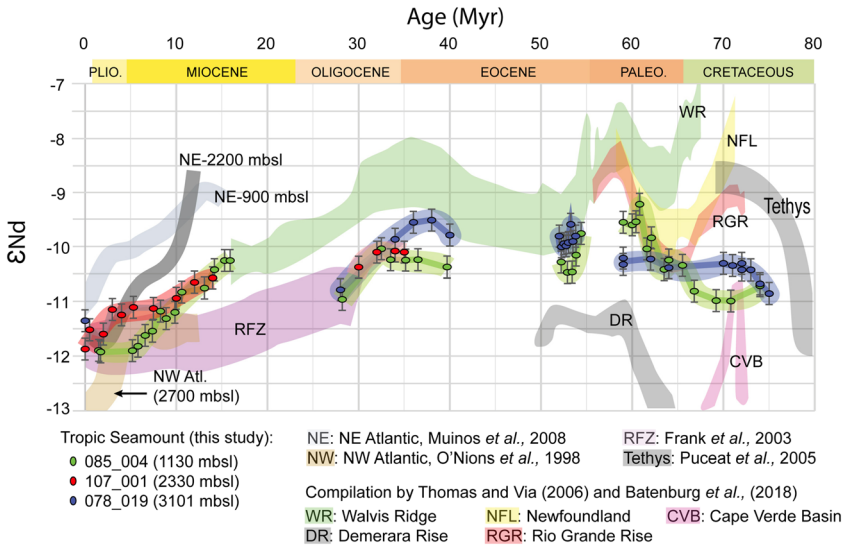

Figure 7. Nd isotope time series for Tropic Seamount samples. Color coding for Nd data from the literature for Fe-Mn crusts and sedimentary records matches Figure 1.

4. Discussion

4.1. Correlated Stratigraphy

The development and optimization of LA-MC-ICP-MS measurements, in a continuous transect across the stratigraphy of Fe-Mn crust samples, allows for the rapid production of high-resolution Pb isotopic profiles. With a laser scan speed of 10 μm/s, a 15 cm traverse can be completely analyzed in just over 4 hr. This method allows for the rapid production of large isotope data sets, opening up new approaches to isotope studies on Fe-Mn crusts. Development of a high-resolution correlated stratigraphy, spanning a complete water depth transect and varied depositional environments on Tropic Seamount (Lusty et al., 2018), permits a robust comparison of the stratigraphy and allows to quantify the influence of environmental factors affecting crust distribution and their mineral textures.

4.1.1. Growth Rate Variability

It is possible to quantify with confidence the variability in growth rate of the Fe-Mn crusts at Tropic Seamount (Figure 3 and Table 3). The most significant difference is observed in the 0–3 and 52–55 Ma

Table 3
Thickness (in mm) of Layers 1–10 of Fe-Mn Crust Samples From Tropic Seamount Based on the Correlated Stratigraphy (Figure 3)

Layer #	Samples								Age (Ma)	Growth rate (mm/Ma)
	083_001	083_007	078_019	078_023	107_001	107_005	085_001	089_010		
1	8	12	4	3*	9	5	2*	2*	0–3	1.3–4.0
2	8	8*	2*	9	14	13	4*	17	3–5	4.5–8.5
3	13	—	—	21	15	14*	22	16	5–10	2.6–4.4
4	31	—	—	31	20		22	20	10–16	3.3–5.2
5	6*	16	8	17	12		14	4*	25–35	0.8–1.7
6	4*	11	14	20	16*		26		35–42	1.6–3.7
7	56	13*	41	6*			21		52–56	5.3–14.0
8			15				22		58–65.5	2.0–2.9
9			7				8		65.5–70	1.6–1.8
10			18				14		70–75	3.0–3.6

Note. The new temporal constraints make it possible to evaluate the range of average growth rate for contemporaneous layers from different samples. Note that thickness measurements marked by an "*" have not been taken into consideration in growth rate calculations due to the effect of the hiatuses or erosive surfaces present. Layers indicated by a "—" are completely absent from the samples.

stratigraphic intervals, where no hiatuses are detectable. There, the growth rates can vary by a factor of 3 between samples separated by less than 4 km. Growth rate variation by a factor 2 is common in most other layers.

The varying growth rates between contemporaneous layers is also reflected in the different textures of each sample. Textures in Fe-Mn crusts have been commonly related to current energy and the associated abundance of sediment available to the actively growing Fe-Mn crust surface (Hein et al., 1992). Notably, laminated textures result from strong currents, which cause the surface on which crusts are accreting to remain particle free (Josso et al., 2020). Varied columnar textures, ranging from densely packed or joined columns, to columns with obvious intercolumnar space, to completely isolated columns or botryoids in a pelagic carbonate matrix, represent decreasing levels of current energy, respectively. Here it is observed that contemporaneous layers have different textures and establishing a correlated stratigraphy solely based on textural data is complex.

However, it is observed that all Tropic Seamount samples present a coherent stratigraphy with regard to changing texture in relation to the energy of the environment of deposition and abundance of detrital particles. Occasionally, specific horizons with obvious textural features can be tracked across the entire water depth transect in all samples. This is notably illustrated by two 3–5 mm thick dense horizons in Layers 2 and 3 of the stratigraphy (Figure 3 and supporting information Figure S7).

4.1.2. The Influence of Phosphatization

Paleoceanographic reconstructions based on isotope data obtained from phosphatised Fe-Mn crust samples have always been treated with caution. Indeed, based on leaching experiments, Koschinsky et al. (1997) indicated that suboxic impregnation of crusts by carbonate fluorapatite (CFA) and the resulting partial dissolution and recrystallization of Fe-Mn oxides may result in alteration of the primary Pb and Nd isotopic signal. Phosphatization occurs during periods of increased upwelling of nutrient-rich deep waters along the flanks of seamounts or continental margins, causing a sudden increase in bioproductivity. This leads to dissolved oxygen depletion and depth expansion of a P_2O_5-rich, oxygen minimum zone (OMZ). These chemical conditions prevent further Fe-Mn oxide precipitation, and impregnation of the existing substrate (volcanics, sedimentary rocks, and Fe-Mn crusts) by CFA, with partial replacement of carbonates. Despite this issue, many authors have conducted isotope studies on phosphatised Fe-Mn crust samples, using the justification that no visible shift in the Nd, Pb, Tl, and Os isotope records is observed at the phosphatized-unphosphatized transition (Christensen et al., 1997; Klemm et al., 2005; Ling et al., 1997; Rehkämper et al., 2004).

Recent work on the geochemical partitioning of Pb in Fe-Mn oxides (Takahashi et al., 2007) and the careful reexamination of leaching experiments by Mizell, Hein, Koschinsky, et al. (2020), demonstrated that the conclusions of Koschinsky et al. (1997) were biased by Pb high reactivity and its readsorption onto the residual phase during the leaching experiment.

The similarity in the contemporaneous (75–38 Ma) Pb isotope trends between the phosphatized 085_004 and unphosphatized 078_019 samples from Tropic Seamount forms a simple demonstration and further evidence of the absence of effect of diagenetic phosphatization on the Pb isotope signature of Fe-Mn crusts in support of the conclusions of Mizell, Hein, Koschinsky, et al. (2020).

4.2. Paleoceanographic Interpretation

The Cenozoic has seen the evolution of Earth's climate from the warm conditions dominating since the Cretaceous and lasting until the mid-Miocene to the high-frequency glacial-interglacial cycles that have dominated the past 2.7 Ma. This transition was in part the result of long trends in cooling and warming but also the result of short, abrupt events, both contemporaneous with a dramatic evolution of the ocean basin configuration (Figure 1) (Thomas & Via, 2006; Wright & Miller, 1996; Zachos et al., 2001). Elucidating past changes in deep-ocean circulation, their timing and origin based on a variety of proxy is therefore essential to reconstruct and improve our understanding of Earth's climate. In this context, Fe-Mn crusts deposits from the northeast Atlantic Tropic Seamount are well positioned to record the influence of Tethyan seawater in the north Atlantic, the onset of NCW, and its circulation between the northwest and northeast Atlantic basins, the timing and effect of the Miocene cooling on the aridification of North Africa as well as the Northern Hemisphere Glaciation.

Most major climatic and geologic events in the Cenozoic evidenced by isotopic $\delta^{13}C$ and $\delta^{18}O$ excursions are matched by a sudden changes or inflections in our Pb isotope data followed by a period of stasis or coincide with the major hiatuses of the Fe-Mn crust deposits (Figure 5). This is notably remarkable at the K-Pg transition, the $\delta^{13}C$ and $\delta^{18}O$ inflection at 62 Ma, the Paleocene-Eocene Thermal Maximum (PETM), Early and Middle Eocene Climate Optimum (EECO and MECO), the apparition of Antarctic ice sheets, Oi-1, and the Northern Hemisphere Glaciation (NHG). This highlights the sensitivity of our record to major climatic variations through the strong feedback of climate on the weathering and transport of Pb from the continental masses to the ocean. Furthermore, the climate-oceanography relationship leading to either accumulation, absence of deposition or erosion of Fe-Mn crusts is well illustrated in this record. Indeed, major positive $\delta^{13}C$ excursions are associated with massive burial of organic carbon caused by enhanced marine productivity, most notably during the Paleocene Carbon Isotope Maximum (~58 Ma; Figure 5). Such conditions are consistent with no Fe-Mn oxide deposition and hiatuses in our composite record. Furthermore, the abrupt Pb isotope variations in the Late Campanian and Maastrichtian could match the high-amplitude cooling and warming events recorded in numerous deep-sea records in the North and South Atlantic, Pacific, and Indian Oceans (Westerhold et al., 2011).

4.2.1. From an Isolated Basin to Open Ocean Record

Deep water Nd data from Tropic Seamount for the Late Cretaceous diverge significantly from the otherwise consistent trends from the Walvis Ridge, Rio Grande Rise and Newfoundland (Figures 1 and 7). The contrast with geographically proximal sediment records from the Cape Verde Basin and Demerara Rise is even more pronounced. A clear Nd Tethys Ocean signal is apparent in the trend of the deep Fe-Mn crusts from Tropic Seamount in the Late Cretaceous, consistent with longitudinal oceanic circulation dominating this region of the proto-North Atlantic basin at this period. However, the disagreement between Tropic Seamount Nd data and other open-ocean records suggests that Tropic Seamount was isolated from the main oceanic circulation occurring at this time at the Walvis Ridge, Rio Grande Rise, and Newfoundland or that the influence of Tethys seawater was localized. Alternatively, in the proto-North Atlantic Ocean, the contact area between the ocean water and its continental margins would have been significant relative to its volume. Accordingly, the large amplitude of variation observed in the Nd data can be attributed to a water column that is strongly influenced by boundary exchange at basin continental margins (Batenburg et al., 2018; Lacan & Jeandel, 2005b). The large spread of Nd values in sediment records from the Demerara Rise and Cape Verde basin (Figure 7), which are geographically proximal to Tropic Seamount, support the strong regional influence of continental sediment input from the ancient cratonic terranes of Africa and South America. These end-members resulted in nearshore sediments having a strongly less radiogenic Nd signature that could influence water column chemistry if deep water circulation was slow and/or the site was located in a small isolated basin (Batenburg et al., 2018). This provides an alternative solution to explain the less radiogenic Tethys-like signature and is consistent with the most radiogenic Pb isotope data observed in Tropic Seamount samples. In addition, the lack of covariation of $^{206}Pb/^{204}Pb$ with the flat-lying $^{207}Pb/^{204}Pb$ ratio (Figure 6), further designates the proximal western and central African cratons as the dominant source of Pb to Tropic Seamount for the period 75–58 Ma. The high-amplitude variations observed in the Pb isotope record of the Late Cretaceous and Paleocene at Tropic Seamount are consistent with the dramatic shifts of the climate and carbon cycles in a period of elevated greenhouse gas levels (Figure 5; Westerhold et al., 2011) and the weathering feedback of continental masses delivering Pb to the ocean.

Given the regional setting, and the warm climatic conditions during the Paleogene, there is much evidence to suggest that the high southern latitudes were the dominant source region for deep water formation during this period (SCW; Batenburg et al., 2018; Thomas & Via, 2007). As the subsidence of the Rio Grande Rise and Walvis ridge continued, and the proto-North Atlantic opened in the Paleocene, deep water circulation was enhanced and proportionally reduced the influence of nearshore processes, causing the Tropic Seamount isotope record to acquire the common water mass signature of the contemporaneous Atlantic. The excursion in εNd observed at 64–58 Ma could represent this convergence toward a Walvis Ridge signature. Alternatively, it could be caused by increased volcanic activity associated with North Atlantic rifting and early eruptive stages of the North Atlantic Igneous Province (62–61 Ma), releasing large quantities of radiogenic Nd into the seawater during the eruptive stages and from weathering of the young basaltic rocks (Batenburg et al., 2018).

4.2.2. Transition From South to NADW Masses

Few isotope records from Fe-Mn crusts are available for the Eocene to Oligocene period, which was a critical period in ocean basin development. Distinct tectonic and isotopic evidences suggest the onset of NCW production either in the Early Oligocene or Early Miocene (Wright et al., 1992). The Oligocene data produced in this study fall between the range of Nd values reported from the Walvis Ridge, the northwest Atlantic basin, and the Romanche fracture zone (RFZ; Figures 1 and 7). During this period, the convergence of Nd isotope data toward less radiogenic values at the Walvis ridge and in the North Atlantic is considered as the marker for increasing contribution of NCW in the Southern Ocean. This feature is clearly visible in the Nd data from the deepest sample from Tropic Seamount. In contrast, the shallower samples have a homogenous signature (−10 to −10.4 ƐNd) during the Late Eocene, indicating the potential influence of shallow water processes or stratification of the water column. Deep, intermediate, and shallow records converge at about 32 Ma and trend toward less radiogenic values that are associated with the onset of NCW. The exact timing and mechanism for this are contentious (Thomas & Via, 2006) with climatic or tectonic driving parameters being possible causes for the initiation of downwelling water masses in the North Atlantic basin. Climatic conditions in the North Atlantic were not thought to be cold enough to trigger thermohaline downwelling until the Early Miocene (Thomas & Via, 2006). Equally, the shift to less radiogenic Nd from about 36–34 Ma in the deepest Fe-Mn crust from Tropic Seamount, and data from Walvis Ridge (Figure 7), correlates well with the deepening of sills between the Norwegian-Greenland Sea and the rest of the North Atlantic 35 Ma ago (Davies et al., 2001). This would have released deeper, less radiogenic Arctic waters into the North Atlantic and this contribution is invoked as the reason for the excursion at Walvis Ridge, highlighting the presence of NCW in the South Atlantic basin as early as 35 Ma (Thomas & Via, 2006). Additionally, this transition from SCW to NCW in the northeast Atlantic basin about 35 Ma is also marked by an inflection in the Pb isotope signature of all the Tropic samples toward more radiogenic values (Figure 5). The Nd and Pb data from Tropic Seamount is therefore in good agreement with an Oligocene onset of NCW production, significantly earlier than previously suggested Miocene estimates supported by C and O isotopes (Wright et al., 1992; Wright & Miller, 1996).

The steep, less radiogenic, Nd excursion in the Oligocene record from Tropic Seamount (34–28 Ma) corresponds with the field of values reported for the Romanche Fracture Zone (−11 ƐNd), which is significantly less radiogenic than other records from the northwest Atlantic from the same period. It is thought that equatorial fracture zones, such as the Romanche or Vema fracture zone (RFZ and VFZ, respectively; Figure 1), were the main locations for the mixing of deep waters from the southern and northwest Atlantic Ocean, upon entering the northeast Atlantic basin. However, the relatively constant Pb and Nd isotope records of deep waters in the fracture zones over the last 33 Ma do not support this simple model of the mixing of NCW and SCW in these locations (Figures 5–7; Frank et al., 2003). In contrast, this signature suggests the nearby Orinoco and Amazon rivers (or their precursors) were the primary sources of Pb and Nd, overprinting any contribution from NCW and/or SCW, and explaining the divergence with Fe-Mn crust records in the northwest Atlantic. The clearly different slope in the $^{207}Pb/^{204}Pb$ ratio at Tropic Seamount for the period 56–25 Ma (Figure 6c) is consistent with an increased contribution of Amazon and Orinoco Pb to the East Atlantic compared to the other periods of the record (Figure 6g). Given that the Orinoco has an ƐNd of −14 and the Amazon has an ƐNd range of −9.2 to −11.4 (Frank et al., 2003), the mixing of these two components could result in the −12 to −10.5 ƐNd signature observed in the RFZ over the last 33 Ma. This signature would be a matching end-member for the influx of Amazon influenced NCW in the eastern Atlantic basin to explain the Nd isotope evolution at Tropic Seamount. An absence of Fe-Mn crusts or sedimentary Nd data from the northeast Atlantic basin over the period 30–15 Ma prevents evaluation of the potential presence of NCW influx into the eastern Atlantic basin via a northern route.

During the Neogene (from 17 Ma to present), Nd records from the NW Atlantic basin present similar trends, with a relatively constant signature until 3 Ma where a strong excursion to less radiogenic values is initiated (Figure 7). This sudden change has been attributed to a new influence on the NCW from LSW, redefining it as the modern NADW. It has been suggested that this period marks the onset of deep water production in the Labrador Sea, bringing less radiogenic (−16 to −14.1 ƐNd) in the NCW from the Canadian Shield, in response to the closure of the Panama gateway (Blaser et al., 2020; Lacan & Jeandel, 2005b; Lambelet et al., 2016; Reynolds et al., 1999). Evidences from Fe-Mn crust records in the NE Atlantic basin highlight a decoupled unradiogenic Nd and radiogenic Pb signature from the NW Atlantic basin up to 12 Ma (Abouchami

et al., 1999; Muiños et al., 2008). Our data confirm these trends and extend them back to 15–16 Ma, confirming a decoupled source of NCW in the eastern basin, or at least a different interplay of water masses. These distinct trends between western and eastern north Atlantic basins suggest either (i) contribution from LSW to the eastern basin through a northern route, probably the Charlie-Gibbs Fracture Zone, as proposed by Muiños et al. (2008), or (ii) that the composition of overflowing waters from the ISOW and/or DSOW flowing into the NE basin (Figure 1) were different at this period, probably influenced by old Scandinavian shield lithologies (Abouchami et al., 1999). In both scenarios, the NE Atlantic was ventilated by NCW entering from the north rather than through equatorial fracture zones as was the case for the period 56–25 Ma. While deeper records from the Madeira-Tore Rise (4,600 mbsl) demonstrate limited amplitude of variation for the same period, it is suggested these were influence by SCW admixed with overlying NCW (Muiños et al., 2008). For comparison, the contemporaneous Nd signature of Fe-Mn crusts recovered from the Iberian margins at similar depth show a clear NCW signature, which suggests the restrictions of SCW to the central abyssal part of the northeast Atlantic and confirms the validity of our NCW record at Tropic Seamount.

4.2.3. Influence and Timing of the North African Aridification Event

Previous work by Abouchami et al. (1999) on Fe-Mn crusts at Tropic Seamount dismissed the influence of Saharan dust on the Pb and Nd signature of the region. This was supported by the long held view that riverine discharge is so large relative to the volume of aerosols entering the ocean, and poor-dissolution rate of air-borne particles, that contributions of aerosols to the total ocean budget is negligible, illustrated by the absence of measurable impact of the Asian dust plume on the Pacific Ocean Nd budget (Jones et al., 1994). However, it has also been shown that up to 20% of the Nd contained in Saharan dust particles effectively transfers to surface seawater of the Atlantic Ocean and contributes to the upper water signature, because of the low riverine input from the adjacent desert region (Tachikawa et al., 1997; Tachikawa, Jeandel, Vangriesheim, & Dupré, 1999). The divergence in Nd signature in samples from Tropic Seamount collected at different water depths at about 7–8 Ma, supports this. The less radiogenic Nd signature of Saharan dust ($-14 < \varepsilon Nd < -12$) represents a suitable end-member to explain decoupling of the records from the two water depths. The divergence is also evident in Pb-Pb space, where a shift toward an end-member with higher $^{207,\ 208}Pb/^{204}Pb$ ratios for a similar $^{206}Pb/^{204}Pb$ take place about 7–8 Ma (Figures 6e and 6f). This matches the known Pb isotope composition of Saharan dust (Abouchami & Zabel, 2003; Kumar et al., 2014; Kumar et al., 2018) mixed with the African cratonic end-member and SCW. Although the field of values for African aerosols is large, representing mixing of highly diverse terranes from various region, the Tropic Seamount Pb data trends toward the signature of the more proximal source regions of Mali, Chad, Niger, and Cap Verde. While the Bodele depression is considered the dominant source of dust in Saharan aerosols (Abouchami et al., 2013), it is possible that progressive sorting and mixing with other dust sources along its path westward mitigate the influence of this region's signature on the East Atlantic seawater.

A large amount of geomorphological, astronomical, and paleoclimatic evidence suggests that the Quaternary Ice Age (2.7 Ma ago) was the reason for North Africa desertification and formation of the Sahara. However, dust flux, vegetation archives, and sea surface temperature indicate a major drying and cooling occurred in the Late Miocene and that arid and semiarid conditions were present in North Africa since 8 Ma, albeit no clear excursions in the carbon and oxygen isotope records (Demenocal, 1995; Feakins et al., 2013; Herbert et al., 2016). Furthermore, despite being strongly contested (Kroepelin, 2006), eolian deposits in the Chad Basin dated to 7 Ma ago, have been interpreted as the earliest record of desert conditions in the Sahara (Schuster et al., 2006). Climate modeling of North Africa suggests an even earlier aridification window 7–11 Ma ago, in response to tectonic forcing of the climate due to shrinkage of the Tethys seaway and rise of the Arabic Peninsula in the Tortonian (Zhang et al., 2014). Alternatively, Herbert et al. (2016) suggested a more global origin for this cooling trend based on a coherent drop in sea surface temperature observed since the Tortonian. Both local tectonic forcing and global cooling would have drastically weakened the African summer monsoon, causing a decrease in atmospheric moisture and a significant reduction in North African precipitation, recorded by major shifts in vegetation types in the tropics and subtropics (Herbert et al., 2016; Zhang et al., 2014).

The data presented here suggests that the aridification of North Africa to an environment capable of delivering a volume of aerosols sufficient to influence the Pb and Nd isotopic signature of the adjacent Atlantic Ocean basin happened about 7–8 Ma. This supports the findings of Schuster et al. (2006) and Zhang et al. (2014) that a major step in the aridification of North Africa occurred 7–11 Ma.

4.2.4. Northern Hemisphere Glaciation

The emergence of the Panama Strait initiated 7–4 Ma ago and completed by 3–2.5 Ma ago interrupted the equatorial influx of Pacific waters into the North Atlantic. This resulted in increased transport of salt and heat toward the poles, further enhancing density-driven production of deep waters in the Arctic region, primarily in the Labrador Sea, and formation of the composite NADW circulation pattern with a well-defined Nd radiogenic signature (Blanckenburg & Nägler, 2001).

The onset of northern hemisphere glaciation about 2.7 Ma (von Blanckenburg & Nägler, 2001) delivered a large amount of detrital material derived from the Canadian Shield to the Labrador basin and resulted in the less radiogenic Nd and radiogenic Pb excursion of NADW through mixing of LSW with ISOW and DSOW (Blanckenburg & Nägler, 2001; Reynolds et al., 1999). This change in inputs and signature of the main water mass bathing the deep Atlantic is clearly evident in Fe-Mn crusts from the northwest Atlantic, and at Tropic Seamount. This more vigorous flux of less radiogenic Nd into the Atlantic, at 3 Ma, could be invoked to explain the sudden excursion in Sample 107_001 from −11 to −12 ƐNd between 3 and 0 Ma, while its ƐNd signature was relatively constant between 7 and 3 Ma. Furthermore, all LA profiles from Tropic Seamount demonstrate an abrupt excursion to more radiogenic $^{206,\ 208}Pb/^{204}Pb$ values (0.7% and 0.3% change, respectively) over the last 3 Ma (Figure 5). In the context of Northern Hemisphere glaciation, the influence of Saharan dust on the surficial water column could have been enhanced over this more recent period. However, the Pb isotope array over 3–0 Ma is clearly trending away from the Saharan dust field toward the signature of NADW (Figure 6). This suggests minor, if not negligible, influence of North African aerosols on the Pb isotope signature of modern NADW.

5. Conclusions

This study presents new time series data for the Pb and Nd isotope evolution of water masses in the northeast Atlantic over the Late Cretaceous and Cenozoic. The use of LA-MC-ICP-MS for Pb isotope analysis of Fe-Mn crust stratigraphy enables large data sets to be rapidly generated with a much higher spatial resolution than microdrilled subsamples. A 15 cm transect can be analyzed in 4 hr, at a vertical spatial resolution of 15 μm, which provides new opportunities for exploiting isotopic data, notably for developing accurate correlated stratigraphies in Fe-Mn crusts. This, in turn, enables comparison of contemporaneous layers in different samples of Fe-Mn crust. This study highlights the significant growth rate variability between samples, the development of similar Fe-Mn textures across a depth range of 1,000–3,800 mbsl, and the absence of influence of phosphatization on the Pb isotope signature of Fe-Mn crusts. This approach also addresses the deficiencies inherent with using a single sample for establishing the paleoceanographic record at a given location when hiatuses are abundant.

The new isotope data demonstrates how the water masses around Tropic Seamount have evolved. The early environment was an isolated basin that was strongly influenced by input of radiogenic Pb and less radiogenic Nd from continental sediments of the West African shelf. This subsequently evolved to a more open ocean environment with progressive change of the Pb-Nd isotopes in the Paleocene from a Tethys to a SCW signature with stronger inputs from the Amazon through circulation via equatorial fracture zones.

A continuously decreasing ƐNd isotope composition suggests LSW or a modified ISOW was influencing the northeast Atlantic basin as early as 15–17 Ma ago at shallow and intermediate water depths. This supports previous interpretations that a northern route for the entry of NCW into the eastern Atlantic existed, rather than being controlled by equatorial fracture zones (Frank et al., 2003; Muiños et al., 2008).

Both Pb and Nd isotopes data record the influence of a new end-member about 7–8 Ma. Its signature matches that of Saharan aerosols providing further support that a major stage of aridification of North African occurred in the Tortonian-Messinian. However, the characteristic signature of Saharan dust is overprinted from 3 Ma to the present by a strong NADW signature related to the onset of Northern Hemisphere glaciation, which introduced greater amounts of less radiogenic Nd and radiogenic $^{206,\ 208}Pb/^{204}Pb$ from Canadian cratonic terranes.

Data Availability Statement

All relevant data to this publication can be access through the British Geological Survey National Geoscience Data Centre (NGDC): Composite Pb isotope record for Tropic Seamount https://doi.org/10.5285/ce4cd06e-ada2-4c2b-89cf-2f0f81884396).

Acknowledgments

P. J., M. H., I. M., and P. L. publish with the permission of the Executive Director, British Geological Survey (UKRI). This research was supported by Natural Environmental Research Council (NERC) Grants NE/M011186/1 (awarded to B. Murton) and NE/M011151/1 (awarded to P. Lusty), which fund the MarineE-Tech project. The authors gratefully thank the reviewers and Editors for their comments, which greatly improved the clarity of the manuscript. The authors also thank the team involved in the RRS James Cook JC142 expedition to Tropic Seamount in 2016.

References

Abbott, A. N., Haley, B. A., & Mcmanus, J. (2016). The impact of sedimentary coatings on the diagenetic Nd flux. *Earth and Planetary Science Letters*, *449*, 217–227. https://doi.org/10.1016/j.epsl.2016.06.001

Abouchami, W., Galer, S. J. G., & Koschinsky, A. (1999). Pb and Nd isotopes in NE Atlantic Fe–Mn crusts: Proxies for trace metal paleosources and paleocean circulation. *Geochimica et Cosmochimica Acta*, *63*(10), 1489–1505. https://doi.org/10.1016/S0016-7037(99)00068-X

Abouchami, W., Näthe, K., Kumar, A., Galer, S. J. G., Jochum, K. P., Williams, E., et al. (2013). Geochemical and isotopic characterization of the Bodélé Depression dust source and implications for transatlantic dust transport to the Amazon Basin. *Earth and Planetary Science Letters*, *380*, 112–123. https://doi.org/10.1016/j.epsl.2013.08.028

Abouchami, W., & Zabel, M. (2003). Climate forcing of the Pb isotope record of terrigenous input into the Equatorial Atlantic. *Earth and Planetary Science Letters*, *213*(3–4), 221–234. https://doi.org/10.1016/S0012-821X(03)00304-2

Baker, J., Peate, D., Waight, T., & Meyzen, C. (2004). Pb isotopic analysis of standards and samples using a 207Pb–204Pb double spike and thallium to correct for mass bias with a double-focusing MC-ICP-MS. *Chemical Geology*, *211*(3–4), 275–303. https://doi.org/10.1016/j.chemgeo.2004.06.030

Batenburg, S. J., Voigt, S., Friedrich, O., Osborne, A. H., Bornemann, A., Klein, T., et al. (2018). Major intensification of Atlantic overturning circulation at the onset of Paleogene greenhouse warmth. *Nature Communications*, *9*(1), 4954. https://doi.org/10.1038/s41467-018-07457-7

Blanckenburg, F., & Nägler, T. F. (2001). Weathering versus circulation-controlled changes in radiogenic isotope tracer composition of the Labrador Sea and North Atlantic Deep Water. *Paleoceanography*, *16*(4), 424–434. https://doi.org/10.1029/2000PA000550

Blaser, P., Gutjahr, M., Pöppelmeier, F., Frank, M., Kaboth-Bahr, S., & Lippold, J. (2020). Labrador Sea bottom water provenance and REE exchange during the past 35,000 years. *Earth and Planetary Science Letters*, *542*, 116299. https://doi.org/10.1016/j.epsl.2020.116299

Christensen, J. N., Halliday, A. N., Godfrey, L. V., Hein, J. R., & Rea, D. K. (1997). Climate and ocean dynamics and the lead isotopic records in Pacific ferromanganese crusts. *Science*, *277*(5328), 913–918. https://doi.org/10.1126/science.277.5328.913

Cochran, J. K., Mckibbin-Vaughan, T., Dornblaser, M. M., Hirschberg, D., Livingston, H. D., & Buesseler, K. O. (1990). ^{210}Pb scavenging in the North Atlantic and North Pacific Oceans. *Earth and Planetary Science Letters*, *97*(3–4), 332–352. https://doi.org/10.1016/0012-821X(90)90050-8

Crosby, A. G., & Mckenzie, D. (2009). An analysis of young ocean depth, gravity and global residual topography. *Geophysical Journal International*, *178*(3), 1198–1219. https://doi.org/10.1111/j.1365-246X.2009.04224.x

Davies, R., Cartwright, J., Pike, J., & Line, C. (2001). Early Oligocene initiation of North Atlantic Deep Water formation. *Nature*, *410*(6831), 917–920. https://doi.org/10.1038/35073551

Demenocal, P. B. (1995). Plio-Pleistocene African Climate. *Science*, *270*(5233), 53–59. https://doi.org/10.1126/science.270.5233.53

Feakins, S. J., Levin, N. E., Liddy, H. M., Sieracki, A., Eglinton, T. I., & Bonnefille, R. (2013). Northeast African vegetation change over 12 m.y. *Geology*, *41*(3), 295–298. https://doi.org/10.1130/G33845.1

Flierdt, T. V. D., Griffiths, A. M., Lambelet, M., Little, S. H., Stichel, T., & Wilson, D. J. (2016). Neodymium in the oceans: A global database, a regional comparison and implications for palaeoceanographic research. *Philosophical Transactions of the Royal Society A: Mathematical, Physical and Engineering Sciences*, *374*(2081), 20150293. https://doi.org/10.1098/rsta.2015.0293

Foster, G. L., & Vance, D. (2006). Negligible glacial–interglacial variation in continental chemical weathering rates. *Nature*, *444*(7121), 918–921. https://doi.org/10.1038/nature05365

Frank, M. (2002). Radiogenic isotopes: Tracers of past ocean circulation and erosional input. *Reviews of Geophysics*, *40*(1), 1001. https://doi.org/10.1029/2000RG000094

Frank, M., van de Flierdt, T., Halliday, A. N., Kubik, P. W., Hattendorf, B., & Günther, D. (2003). Evolution of deepwater mixing and weathering inputs in the central Atlantic Ocean over the past 33 Myr. *Paleoceanography*, *18*(4), 1091. https://doi.org/10.1029/2003PA000919

Frank, M., Whiteley, N., Kasten, S., Hein, J. R., & O'nions, K. (2002). North Atlantic Deep Water export to the Southern Ocean over the past 14 Myr: Evidence from Nd and Pb isotopes in ferromanganese crusts. *Paleoceanography*, *17*(2), 1022. https://doi.org/10.1029/2000PA000606

Godfrey, L. V. (2002). Temporal changes in the lead isotopic composition of red clays: Comparison with ferromanganese crust records. *Chemical Geology*, *185*(3–4), 241–254. https://doi.org/10.1016/S0009-2541(01)00406-5

Goto, K. T., Nozaki, T., Toyofuku, T., Augustin, A. H., Shimoda, G., Chang, Q., et al. (2017). Paleoceanographic conditions on the São Paulo Ridge, SW Atlantic Ocean, for the past 30 million years inferred from Os and Pb isotopes of a hydrogenous ferromanganese crust. *Deep Sea Research Part II: Topical Studies in Oceanography*, *146*, 82–92. https://doi.org/10.1016/j.dsr2.2016.10.010

Haq, B. U. (2014). Cretaceous eustasy revisited. *Global and Planetary Change*, *113*, 44–58. https://doi.org/10.1016/j.gloplacha.2013.12.007

Haq, B. U., Hardenbol, J., & Vail, P. R. (1987). Chronology of fluctuating sea levels since the Triassic. *Science*, *235*(4793), 1156–1167. https://doi.org/10.1126/science.235.4793.1156

Harlavan, Y., & Erel, Y. (2002). The release of Pb and REE from granitoids by the dissolution of accessory phases. *Geochimica et Cosmochimica Acta*, *66*(5), 837–848. https://doi.org/10.1016/S0016-7037(01)00806-7

Hein, J. R., Bohrson, W. A., Schulz, M. S., Noble, M., & Clague, D. A. (1992). Variations in the fine-scale composition of a Central Pacific ferromanganese crust: Paleoceanographic implications. *Paleoceanography*, *7*(1), 63–77. https://doi.org/10.1029/91PA02936

Henderson, G. M., & Maier-Reimer, E. (2002). Advection and removal of 210Pb and stable Pb isotopes in the oceans: A general circulation model study. *Geochimica et Cosmochimica Acta*, *66*(2), 257–272. https://doi.org/10.1016/S0016-7037(01)00779-7

Herbert, T. D., Lawrence, K. T., Tzanova, A., Peterson, L. C., Caballero-Gill, R., & Kelly, C. S. (2016). Late Miocene global cooling and the rise of modern ecosystems. *Nature Geoscience*, *9*(11), 843–847. https://doi.org/10.1038/ngeo2813

Jeandel, C., Arsouze, T., Lacan, F., Téchiné, P., & Dutay, J. C. (2007). Isotopic Nd compositions and concentrations of the lithogenic inputs into the ocean: A compilation, with an emphasis on the margins. *Chemical Geology*, *239*(1–2), 156–164. https://doi.org/10.1016/j.chemgeo.2006.11.013

Jenkins, W. J., Smethie, W. M., Boyle, E. A., & Cutter, G. A. (2015). Water mass analysis for the U.S. GEOTRACES (GA03) North Atlantic sections. *Deep Sea Research Part II: Topical Studies in Oceanography*, *116*, 6–20. https://doi.org/10.1016/j.dsr2.2014.11.018

Jochum, K. P., Nohl, U., Herwig, K., Lammel, E., Stoll, B., & Horfmann, A. (2005). *Geostandards and geoanalytical research*.

Johannesson, K. H., & Burdige, D. J. (2007). Balancing the global oceanic neodymium budget: Evaluating the role of groundwater. *Earth and Planetary Science Letters*, *253*(1–2), 129–142. https://doi.org/10.1016/j.epsl.2006.10.021

Jones, C. E., Halliday, A. N., Rea, D. K., & Owen, R. M. (1994). Neodymium isotopic variations in North Pacific modern silicate sediment and the insignificance of detrital REE contributions to seawater. *Earth and Planetary Science Letters*, *127*(1–4), 55–66. https://doi.org/10.1016/0012-821X(94)90197-X

Josso, P., Parkinson, I., Horstwood, M., Lusty, P., Chenery, S., & Murton, B. (2019). Improving confidence in ferromanganese crust age models: A composite geochemical approach. *Chemical Geology*, *513*, 108–119. https://doi.org/10.1016/j.chemgeo.2019.03.003

Josso, P., Rushton, J., Lusty, P., Matthews, A., Chenery, S., Holwell, D., et al. (2020). Late Cretaceous and Cenozoic paleoceanography from north-east Atlantic ferromanganese crust microstratigraphy. *Marine Geology*, *422*, 106122. https://doi.org/10.1016/j.margeo.2020.106122

Katz, M. E., Cramer, B. S., Toggweiler, J. R., Esmay, G., Liu, C., Miller, K. G., et al. (2011). Impact of Antarctic circumpolar current development on late Paleogene ocean structure. *Science*, *332*(6033), 1076–1079. https://doi.org/10.1126/science.1202122

Klemm, V., Levasseur, S., Frank, M., Hein, J. R., & Halliday, A. N. (2005). Osmium isotope stratigraphy of a marine ferromanganese crust. *Earth and Planetary Science Letters*, *238*(1–2), 42–48. https://doi.org/10.1016/j.epsl.2005.07.016

Konstantinova, N., Cherkashov, G., Hein, J. R., Mirão, J., Dias, L., Madureira, P., et al. (2017). Composition and characteristics of the ferromanganese crusts from the western Arctic Ocean. *Ore Geology Reviews*, *87*, 88–99. https://doi.org/10.1016/j.oregeorev.2016.09.011

Koschinsky, A., & Hein, J. R. (2017). Marine ferromanganese encrustations: Archives of changing oceans. *Elements*, *13*(3), 177–182. https://doi.org/10.2113/gselements.13.3.177

Koschinsky, A., Stascheit, A., Bau, M., & Halbach, P. (1997). Effects of phosphatization on the geochemical and mineralogical composition of marine ferromanganese crusts. *Geochimica et Cosmochimica Acta*, *61*(19), 4079–4094. https://doi.org/10.1016/S0016-7037(97)00231-7

Kroepelin, S. (2006). Revisiting the age of the Sahara Desert. *Science*, *312*, 1138–1139.

Kumar, A., Abouchami, W., Galer, S. J. G., Garrison, V. H., Williams, E., & Andreae, M. O. (2014). A radiogenic isotope tracer study of transatlantic dust transport from Africa to the Caribbean. *Atmospheric Environment*, *82*, 130–143. https://doi.org/10.1016/j.atmosenv.2013.10.021

Kumar, A., Abouchami, W., Galer, S. J. G., Singh, S. P., Fomba, K. W., Prospero, J. M., & Andreae, M. O. (2018). Seasonal radiogenic isotopic variability of the African dust outflow to the tropical Atlantic Ocean and across to the Caribbean. *Earth and Planetary Science Letters*, *487*, 94–105. https://doi.org/10.1016/j.epsl.2018.01.025

Lacan, F., & Jeandel, C. (2005a). Acquisition of the neodymium isotopic composition of the North Atlantic Deep Water. *Geochemistry, Geophysics, Geosystems*, *6*, Q12008. https://doi.org/10.1029/2005GC000956

Lacan, F., & Jeandel, C. (2005b). Neodymium isotopes as a new tool for quantifying exchange fluxes at the continent–ocean interface. *Earth and Planetary Science Letters*, *232*(3–4), 245–257. https://doi.org/10.1016/j.epsl.2005.01.004

Lambelet, M., van de Flierdt, T., Crocket, K., Rehkämper, M., Kreissig, K., Coles, B., et al. (2016). Neodymium isotopic composition and concentration in the western North Atlantic Ocean: Results from the GEOTRACES GA02 section. *Geochimica et Cosmochimica Acta*, *177*, 1–29. https://doi.org/10.1016/j.gca.2015.12.019

Ling, H. F., Burton, K. W., O'nions, R. K., Kamber, B. S., von Blanckenburg, F., Gibb, A. J., & Hein, J. R. (1997). Evolution of Nd and Pb isotopes in Central Pacific seawater from ferromanganese crusts. *Earth and Planetary Science Letters*, *146*, 1–12.

Lusty, P., Hein, J. R., & Josso, P. (2018). Formation and occurrence of ferromanganese crusts: Earth's storehouse for critical metals. *Elements*, *14*(5), 313–318. https://doi.org/10.2138/gselements.14.5.313

Millot, R., Allègre, C.-J., Gaillardet, J., & Roy, S. (2004). Lead isotopic systematics of major river sediments: A new estimate of the Pb isotopic composition of the Upper Continental Crust. *Chemical Geology*, *203*(1–2), 75–90. https://doi.org/10.1016/j.chemgeo.2003.09.002

Mizell, K., Hein, J. R., Koschinsky, A., & Hayes, S. M. (2020). Effects of phosphatization on the mineral associations and speciation of Pb in ferromanganese crusts. *ACS Earth and Space Chemistry*, *4*(9), 1515–1526. https://doi.org/10.1021/acsearthspacechem.0c00037

Mizell, K., Hein, J. R., Lam, P. J., Koppers, A. A. P., & Staudigel, H. (2020). Geographic and oceanographic influences on ferromanganese crust composition along a Pacific Ocean Meridional Transect, 14 N to 14S. *Geochemistry, Geophysics, Geosystems*, *21*, e2019GC008716. https://doi.org/10.1029/2019GC008716

Mourlot, Y., Roddaz, M., Dera, G., Calvès, G., Kim, J.-H., Chaboureau, A.-C., et al. (2018). Geochemical evidence for large-scale drainage reorganization in Northwest Africa during the Cretaceous. *Geochemistry, Geophysics, Geosystems*, *19*, 1690–1712. https://doi.org/10.1029/2018GC007448

Muiños, S. B., Frank, M., Maden, C., Hein, J. R., van de Flierdt, T., Lebreiro, S. M., et al. (2008). New constraints on the Pb and Nd isotopic evolution of NE Atlantic water masses. *Geochemistry, Geophysics, Geosystems*, *9*, Q02007. https://doi.org/10.1029/2007GC001766

Nishi, K., Usui, A., Nakasato, Y., & Yasuda, H. (2017). Formation age of the dual structure and environmental change recorded in hydrogenetic ferromanganese crusts from Northwest and Central Pacific seamounts. *Ore Geology Reviews*, *87*, 62–70. https://doi.org/10.1016/j.oregeorev.2016.09.004

Paton, C., Hellstrom, J., Paul, B., Woodhead, J., & Hergt, J. (2011). Iolite: Freeware for the visualisation and processing of mass spectrometric data. *Journal of Analytical Atomic Spectrometry*, *26*(12), 2508–2518. https://doi.org/10.1039/c1ja10172b

Pérez-Díaz, L., & Eagles, G. (2017). South Atlantic paleobathymetry since early Cretaceous. *Scientific Reports*, *7*(1), 11819. https://doi.org/10.1038/s41598-017-11959-7

Pucéat, E., Lécuyer, C., & Reisberg, L. (2005). Neodymium isotope evolution of NW Tethyan upper ocean waters throughout the Cretaceous. *Earth and Planetary Science Letters*, *236*(3-4), 705–720. https://doi.org/10.1016/j.epsl.2005.03.015

Rehkämper, M., Frank, M., Hein, J. R., & Halliday, A. (2004). Cenozoic marine geochemistry of thallium deduced from isotopic studies of ferromanganese crusts and pelagic sediments. *Earth and Planetary Science Letters*, *219*(1–2), 77–91. https://doi.org/10.1016/S0012-821X(03)00703-9

Reynolds, B. C., Frank, M., & O'nions, R. K. (1999). Nd- and Pb-isotope time series from Atlantic ferromanganese crusts: Implications for changes in provenance and paleocirculation over the last 8 Myr. *Earth and Planetary Science Letters*, *173*, 381–396.

Rickli, J., Frank, M., & Halliday, A. N. (2009). The hafnium–neodymium isotopic composition of Atlantic seawater. *Earth and Planetary Science Letters*, *280*(1–4), 118–127. https://doi.org/10.1016/j.epsl.2009.01.026

Scher, H. D., & Martin, E. E. (2008). Oligocene deep water export from the North Atlantic and the development of the Antarctic Circumpolar Current examined with neodymium isotopes. *Paleoceanography*, *23*, PA1205. https://doi.org/10.1029/2006PA001400

Scher, H. D., Whittaker, J. M., Williams, S. E., Latimer, J. C., Kordesch, W. E. C., & Delaney, M. L. (2015). Onset of Antarctic Circumpolar Current 30 million years ago as Tasmanian Gateway aligned with westerlies. *Nature*, *523*(7562), 580–583. https://doi.org/10.1038/nature14598

Schlitzer, R., Anderson, R. F., Dodas, E. M., Lohan, M., Geibert, W., Tagliabue, A., et al. (2018). The GEOTRACES intermediate data product 2017. *Chemical Geology*, *493*, 210–223. https://doi.org/10.1016/j.chemgeo.2018.05.040

Schuster, M., Duringer, P., Ghienne, J.-F., Vignaud, P., Mackaye, H. T., Likius, A., & Brunet, M. (2006). The age of the Sahara Desert. *Science*, *311*(5762), 821–821. https://doi.org/10.1126/science.1120161

Scotese, C. R. (2016). PALEOMAP PaleoAtlas for GPlates and the PaleoData plotter program, PALEOMAP Project. Accessible on: http://www.earthbyte.org/paleomap-paleoatlas-for-gplates/

Sun, S.-S., Bailey, D. K., Tarney, J., & Dunham, K. C. (1980). Lead isotopic study of young volcanic rocks from mid-ocean ridges, ocean islands and island arcs. *Philosophical Transactions of the Royal Society of London. Series A. Mathematical and Physical Sciences*, *297*, 409–445.

Tachikawa, K., Handel, C., & Dupré, B. (1997). Distribution of rare earth elements and neodymium isotopes in settling particulate material of the tropical Atlantic Ocean (EUMELI site). *Deep Sea Research Part I: Oceanographic Research Papers*, *44*(11), 1769–1792. https://doi.org/10.1016/S0967-0637(97)00057-5

Tachikawa, K., Jeandel, C., & Roy-Barman, M. (1999). A new approach to the Nd residence time in the ocean: The role of atmospheric inputs. *Earth and Planetary Science Letters*, *170*(4), 433–446. https://doi.org/10.1016/S0012-821X(99)00127-2

Tachikawa, K., Jeandel, C., Vangriesheim, A., & Dupré, B. (1999). Distribution of rare earth elements and neodymium isotopes in suspended particles of the tropical Atlantic Ocean (EUMELI site). *Deep Sea Research Part I: Oceanographic Research Papers*, *46*(5), 733–755. https://doi.org/10.1016/S0967-0637(98)00089-2

Takahashi, Y., Manceau, A., Geoffroy, N., Marcus, M. A., & Usui, A. (2007). Chemical and structural control of the partitioning of Co, Ce, and Pb in marine ferromanganese oxides. *Geochimica et Cosmochimica Acta*, *71*(4), 984–1008. https://doi.org/10.1016/j.gca.2006.11.016

Tanaka, T., Togashi, S., Kamioka, H., Amakawa, H., Kagami, H., Hamamoto, T., et al. (2000). JNdi-1: A neodymium isotopic reference in consistency with LaJolla neodymium. *Chemical Geology*, *168*(3–4), 279–281. https://doi.org/10.1016/S0009-2541(00)00198-4

Thomas, D. J., & Via, R. K. (2006). Evolution of Atlantic thermohaline circulation: Early Oligocene onset of deep-water production in the North Atlantic. *Geology*, *34*, 441–444.

Thomas, D. J., & Via, R. K. (2007). Neogene evolution of Atlantic thermohaline circulation: Perspective from Walvis Ridge, southeastern Atlantic Ocean. *Paleoceanography*, *22*, PA2212. https://doi.org/10.1029/2006PA001297

van den Bogaard, P. (2013). The origin of the Canary Island Seamount Province—New ages of old seamounts. *Scientific Reports*, *3*, 1–7.

Westerhold, T., Röhl, U., Donner, B., Mccarren, H. K., & Zachos, J. C. (2011). A complete high-resolution Paleocene benthic stable isotope record for the central Pacific (ODP Site 1209). *Paleoceanography*, *26*, PA2216. https://doi.org/10.1029/2010PA002092

Wright, J. D., & Miller, K. G. (1996). Control of North Atlantic Deep Water Circulation by the Greenland-Scotland Ridge. *Paleoceanography*, *11*(2), 157–170. https://doi.org/10.1029/95PA03696

Wright, J. D., Miller, K. G., & Fairbanks, R. G. (1992). Early and Middle Miocene stable isotopes: Implications for Deepwater circulation and climate. *Paleoceanography*, *7*(3), 357–389. https://doi.org/10.1029/92PA00760

Yeo, I., Dobson, K., Josso, P., Pearce, R., Howarth, S., Lusty, P., et al. (2018). Assessment of the mineral resource potential of Atlantic ferromanganese crusts based on their growth history, microstructure, and texture. *Minerals*, *8*(8), 327. https://doi.org/10.3390/min8080327

Yeo, I. A., Howarth, S. A., Spearman, J., Cooper, A., Crossouard, N., Taylor, J., et al. (2019). Distribution of and hydrographic controls on ferromanganese crusts: Tropic Seamount, Atlantic. *Ore Geology Reviews*, *114*, 103131. https://doi.org/10.1016/j.oregeorev.2019.103131

Zachos, J., Pagani, M., Sloan, L., Thomas, E., & Billups, K. (2001). Trends, rhythms, and aberrations in global climate 65 Ma to present. *Science*, *292*(5517), 686–693. https://doi.org/10.1126/science.1059412

Zachos, J. C., Dickens, G. R., & Zeebe, R. E. (2008). An early Cenozoic perspective on greenhouse warming and carbon-cycle dynamics. *Nature*, *451*(7176), 279–283. https://doi.org/10.1038/nature06588

Zhang, Z., Ramstein, G., Schuster, M., Li, C., Contoux, C., & Yan, Q. (2014). Aridification of the Sahara desert caused by Tethys Sea shrinkage during the Late Miocene. *Nature*, *513*(7518), 401–404. https://doi.org/10.1038/nature13705